

MOLECULAR DYNAMICS SIMULATION OF THE MESOPHASE BEHAVIOR  
OF THERMOTROPIC BOLAAMPHIPHILES WITH A SWALLOW-TAIL  
LATERAL CHAIN

A Thesis

Presented to the Faculty of the Graduate School  
of Cornell University

In Partial Fulfillment of the Requirements for the Degree of  
Master of Science

by

Yangyang Sun

August 2017

© 2017 Yangyang Sun

## ABSTRACT

Recent experimental studies have shown that T-shaped bolaamphiphiles (TBA) with a swallow-tail lateral chain display several thermotropic liquid crystalline phases depending on the size of the lateral chain and temperature. In this work, we use molecular simulations of a simple coarse-grained model to map out the phase behavior of this type of molecules. This model is based on the premise that the crucial details of the fluid structure stem from close range repulsions and the strong directional force typical of hydrogen bonds. Our simulations confirm that TBAs exhibit a rich phase behavior upon increasing the length of their lateral chain. The simulations successfully detect the double gyroid phase and the axial-bundle columnar phase, whose structures are similar to those found in experiment. In addition, simulations predict two cocontinuous phases with 3D-periodicity (the “single” diamond and the “single” plumber’s nightmare phase) yet to be reported in experimental studies. The structure factor and several 2D order parameters are used to identify and characterize these liquid crystal phases. D1.avi and P1.avi are provided as supplementary materials to confirm that these ordered phases have some fluidity consistent with a liquid crystal character.

## BIOGRAPHICAL SKETCH

Yangyang Sun was born in Yima, Henan, China in the year 1994. He got his Bachelor of Engineering degree in Macromolecule Material & Engineering from Beijing Institute of Technology in 2015. He received his Chemical Engineering M.Eng. degree from Cornell University in 2016. He did his M.Eng. project at Prof. Fernando A. Escobedo's lab at Cornell University, and decided to continue his graduate studies to pursue a M.S. degree. Under Prof. Escobedo's guidance, he worked on simulating the mesophase behavior of the self-assembling liquid crystal molecules.

## ACKNOWLEDGMENTS

I would like to thank my thesis advisor Prof. Fernando A. Escobedo of the Robert Frederick Smith School of Chemical and Biomolecular Engineering at Cornell University. The door to Prof. Escobedo office was always open for me when I had question about my research or writing. His constant guidance and support encouraged me to continue my graduate studies and pursue the M.S. degree. I would like to thank Prof. Paulette Clancy for useful discussions and always being encouraging throughout the duration of this project. I would like to thank Prof. Christopher Kemper Ober for helping me bridge the gap between the experiment and the simulation. I am also grateful to Dr. Poornima Padmanabhan for providing the code and guidance to start this project and many helpful discussions. I would also like to thank Dr. Mayank Misra, Endian Wang and Christian Nowak for helpful discussions and guidance. I would like to acknowledge the funding supported by the National Science Foundation Award DMR-1629369 and DMR-2609997. This work used the Extreme Science and Engineering Discovery Environment (XSEDE), which is supported by National Science Foundation grant number ACI-1053575.

Finally, I must express my very profound gratitude to my parents for providing me with unfailing support and continuous encouragement throughout my years of study. This accomplishment would not have been possible without them.

## TABLE OF CONTENTS

BIOGRAPHICAL SKETCH.....	iii
ACKNOWLEDGMENTS.....	iv
TABLE OF CONTENTS.....	v
1 INTRODUCTION.....	1
2 METHODOLOGY.....	6
2.1 Molecular model.....	6
2.2 Analysis methods for 2D columnar phases.....	12
2.3 Analysis methods for 3D periodic order phases.....	14
2.4 The mobility coefficient.....	16
3 RESULTS.....	18
3.1 Global phase diagram.....	18
3.2 2D and 3D periodic phases.....	20
3.3 Comparison of linear vs. swallow-tail TBAs.....	32
4 CONCLUSIONS.....	36
APPENDIX.....	38
REFERENCE.....	48

## CHAPTER 1

### INTRODUCTION

Liquid crystals (LCs) are one of the most important types of self-assembling soft materials for both scientific research and commercial applications. In LC phases, the self-assembly ability of the constituent molecules arises from some anisotropy in the interparticle interactions[1]. In poly-amphiphilic molecules, for example, self-assembly is aided by the nanosegregation that occurs between incompatible segments, such as rigid and flexible segments or hydrophilic and hydrophobic segments[1]. In addition to self-assembling into nanoscale or mesoscale ordered structures, these molecules also retain a liquid-like mobility to change their position and configuration[1]. Often, aromatic rings are present in the rigid segment of LC molecules. The combination of structural order and fluidity allows LCs to develop an orderly and dense packing of  $\pi$ -conjugated systems over large areas without sharp grain boundaries, a property which is crucial for applications involving charge carrier transport[2]. Indeed, LCs have become promising organic semiconductors[2-5]. LCs can also host other non-mesogenic units (polymers, metallic nanoparticles) to assist them to form desired morphologies, and the resulting composite materials can be used as mechanical actuators[6] and plasmonic metamaterials[7,8]. But for any such application, the performance of LCs depends strongly on the microscopic details of the morphology assembled by the molecules. In order to improve the properties and widen the uses of LCs, significant effort has been devoted to engineer new mesogens and construct new microscopic morphologies.

Bi- and co-continuous cubic phases are of particular interest due to their 3D symmetry with continuous domains of different segment types. Usually, these phases can be described as two interwoven (bicontinuous) networks or a single (cocontinuous) network, of a minority component embedded in the continuous matrix of the majority component[9]. Due to the large internal interfacial area, structural integrity, and mechanical stability of these phases, they can be used as templates and structure-directing agents to fabricate mesoporous materials[10,11], high conductivity matrices[12-14], nanofiltration membranes[15,16], dye-sensitized solar cell[17-19], electrochromic devices[20], photonic crystals and metamaterials[21-23]. Bicontinuous phases are also found in some biological membranes with specialized biophysical properties[24,25]. Currently, bicontinuous and cocontinuous phases have been extensively studied in lyotropic LC systems[26-32] and diblock copolymers[33-36]. However, only a few thermotropic LC systems have been reported to display these 3D-periodic phases, including polycatenars[37-41], wedge-shaped molecules[42,43] and bolaamphiphilics[44,45].

T-shaped bolaamphiphiles “TBAs” have attracted significant attention for their rich phase behavior. Usually, these molecules contain three incompatible segments: the rigid linear biphenyl core, two polar 1,2-diol group at each end, and one laterally attached flexible chain (alkyl chains, or semi-fluorinated chains)[46,47]. By combining both shape anisotropy and amphiphilicity, bolaamphiphiles can self-assemble into complex and new LC phases at particular temperature ranges[1]. Experiments[46,47] have demonstrated the formation of a series of columnar phases with cross-sections having different 2D patterns depending on the size of the lateral chains. Unlike the traditionally

columnar phases formed by round cylinders, these columnar phases exhibit honeycomb patterns formed by different polygonal cylinders ranging from triangular to hexagonal[46,47], where rigid cores form the shell of each cylinder and the lateral chains fill the inside of each cylinder. Since polar end-groups aggregate at the edges of each cylinder, strong hydrogen bonds make this honeycomb structure very stable. Giant honeycomb phases and lamella phases are observed when the TBA side chain size is increased further[46,47]. Recently, experiments[44,45] have shown that attaching a swallow-tail lateral chain to the rigid rods (see example shown in Figure 1) can disrupt the continuous segregated subdomain of the rigid rods found in columnar phases and lamella phases of TBAs, leading to the formation of isolated bundled rigid rods. These axial rod-bundles can form infinite networks embedded in the continuous matrix of lateral chains, sometimes leading to bicontinuous phases.

The presence of three incompatible segments allows TBAs to exhibit a rich phase behavior and to form highly intricate phases; however, the complex chemical structure of TBAs also makes it difficult to establish a molecular design strategy to target specific LC phases. Computer simulation can provide helpful information to understand and predict phase behavior from molecular chemical composition. Nevertheless, fully atomistic molecular simulations of the self-assembly of complex molecules in relatively large systems is still challenging given the limited computational resources typically available. Fortunately, a previous study[48] proved that the mesophases formed by TBAs are largely driven by the overall interaction between incompatible segments, which makes coarse-grained molecular models suitable. Based on the premise that the crucial details of the fluid structure stem from close range repulsions and the strong

directional forces typical of hydrogen bonds, a simple coarse-grained approach was employed by Crane *et al.*[48] Their model treated van der Waals interactions via soft repulsions and strong directional hydrogen bonds as simple attractions. This model was used to describe the phase behavior of TBAs with a linear lateral chain and found to successfully reproduce the different types of honeycombed columnar phases that had been observed in experiments[46, 47].

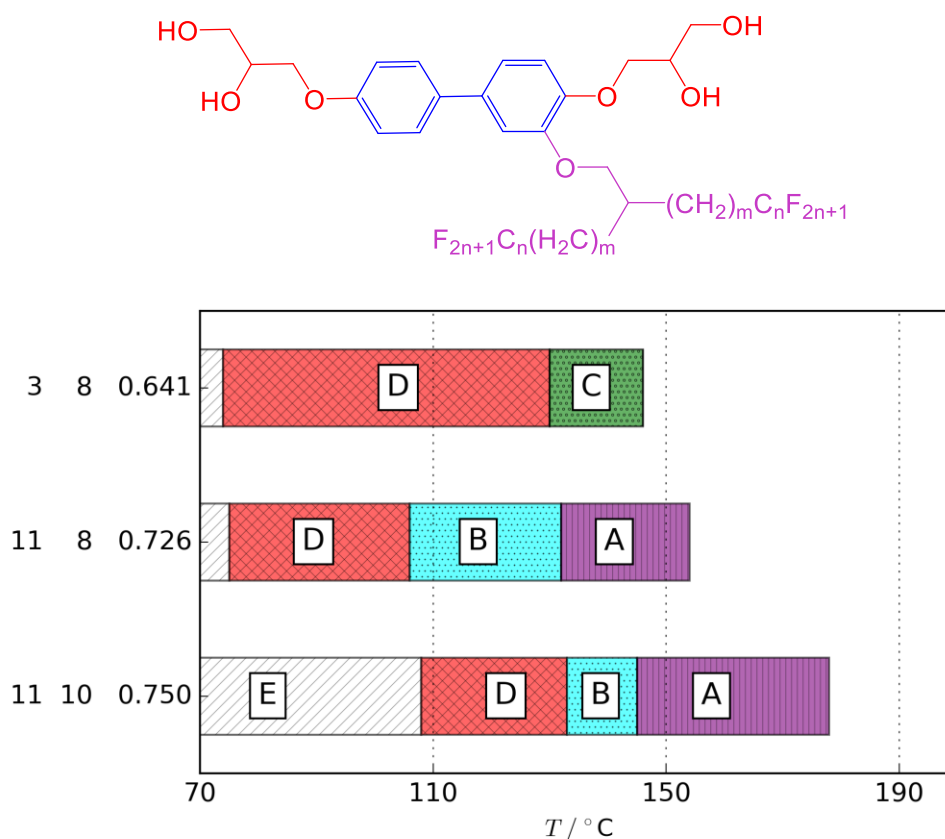


Figure 1 Structure of the core bolaamphiphile molecule with a swallow-tail lateral chain that served as the prototype of this study, and the dependence of the LC experimentally found for this molecule with respect to the length of the lateral chain and the temperature. Phase description: (A) double gyroid LC; (B) axial-bundle columnar liquid crystal; (C) double diamond liquid crystal; (D) lamella LC; (E) crystal. Adapted from ref. 44,45.

In this work, we seek to apply a coarse-grained model akin to that used by Crane *et al.* to simulate the phase behavior of TBAs with a swallow-tail lateral chain of different lengths. Our main goal is to confirm and fill in the gaps in the phase diagram mapped by experiments. Because such TBAs can form complex mesophases with long-range, periodic order, particle-based molecular dynamics simulations are sensitive to finite-size effects, especially for 3D-periodic phases[34,49,50]. Indeed, for such phases to be formed, the simulation box size must be commensurate with an integer number of the phase unit cells. Therefore, the size of simulation box need to be carefully treated as an additional variable to explore in the simulations. Our simulations are able not only to detect a double gyroid phase and axial-bundled columnar phase similar to those recently observed in experiments, but also to predict two novel cocontinuous phases yet to be reported in experimental studies of TBAs (although a similar cocontinuous phase has been reported in a triblock copolymer system[51]).

The rest of this manuscript is organized as follows. Chapter 2 describes the coarse-grained model we adopted, details about how to implement simulations, and tools to determine the ordered phases with different morphologies. Chapter 3 summarizes the phase behavior of TBAs in terms of the reduced temperature and the volume fraction of the lateral chain. Chapter 4 presents our conclusions.

## CHAPTER 2

### METHODOLOGY

#### ***2.1 Molecular model***

We adopt a simple coarse-grained model to study the phase behavior of TBAs with one swallow-tail lateral chain, following the work of Crane *et al.*[48] In this model, the aromatic core and glycerol groups are represented by six beads kept in a rigid linear configuration with an inter-bead distance of  $0.7\sigma$ . The lateral chain has two branches, and is attached to the rigid unit at the third bead (see Figure 2). The length of each branch is  $N_{\text{chain}}$  beads with an inter-bead distance of  $\sigma$ , and the total number of beads in the lateral chain ( $N_{\text{flx}}$ ) is  $(2N_{\text{chain}} + 1)$ . In this work,  $N_{\text{chain}}$  is varied from 1 to 16, corresponding  $N_{\text{flx}}$  from 3 to 33. Here  $\sigma$  is a characteristic length of the model, defined roughly as the diameter of a bead in the TBA. The basic topology of this model is depicted in Figure 2. Bonded interactions act only between beads in the lateral chain and in the link between the lateral chain and the rigid unit, and are described by a harmonic potential of the form

$$U^{\text{har}} = \frac{1}{2}k_{\text{sp}}(r - r_0)^2 \quad (1)$$

where  $r$  is the separation distance between the bonded beads,  $r_0$  is the equilibrium separation, and  $k_{\text{sp}}$  is the spring constant. We set  $r_0 = \sigma$  and  $k_{\text{sp}} = 50(\varepsilon/\sigma^2)$ , where  $\varepsilon$  is a characteristic energy of the model, defined in terms of pair potentials between beads as described later.

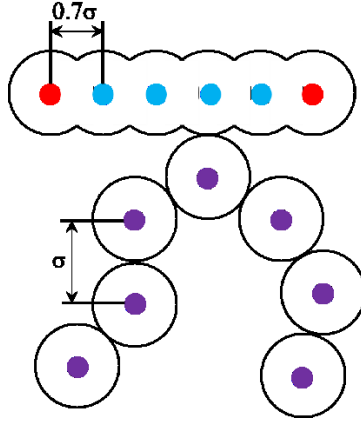


Figure 2 Cartoon of the TBA molecules studied in this work. Type 1 beads, corresponding to hydrogen-bond-like sites, are colored red; type 2 beads, corresponding to the linear biphenyl core of the molecules, are colored in blue; type 3 beads, corresponding to the grafted lateral chains, are colored purple. All beads are the same diameter,  $\sigma$ , and mass. Adapted from ref. 48.

To mimic the chemistry of TBAs, we divided all beads into three different types. Type 1 beads, located at the two ends of the rigid unit, represent strongly attractive hydrogen-bond-like sites. Type 2 beads, constituting the remainder of the rigid unit, represent the biphenyl core. Type 3 beads represent the lateral aliphatic chain. All pair potential energies were defined through the cut and shifted Lennard-Jones potential (CSLJ)

$$U_{AB}^{\text{LJCS}}(r; C_{AB}) = \begin{cases} U_{AB}^{\text{LJ}}(r) - U_{AB}^{\text{LJ}}(C_{AB}) & 0 < r < C_{AB} \\ 0 & r \geq C_{AB} \end{cases} \quad (2)$$

with

$$U_{AB}^{\text{LJ}}(r) = 4\varepsilon_{AB} \left[ \left( \frac{\sigma_{AB}}{r} \right)^{12} - \left( \frac{\sigma_{AB}}{r} \right)^6 \right] \quad (3)$$

$$U_{AB}^{\text{LJ}}(C_{AB}) = 4\varepsilon_{AB} \left[ \left( \frac{\sigma_{AB}}{C_{AB}} \right)^{12} - \left( \frac{\sigma_{AB}}{C_{AB}} \right)^6 \right] \quad (4)$$

where A and B represent the bead type,  $r$  is the bead separation,  $\varepsilon_{AB}$  describes the depth of the potential well,  $\sigma_{AB}$  is the distance where the inter-particle potential is zero,  $C_{AB}$  is the cut-and-shifted distance. The  $\varepsilon_{AB}$  and  $C_{AB}$  parameters used in each type of pair potential are summarized in Table 1; all beads have the same value of  $\sigma_{AB} = \sigma$ . Only self-interactions of type 1 and type 3 beads have the attractive part but with different strength. All the cross interactions and interactions between type 2 beads have a cut-off distance of  $C_{AB} = 2^{1/6}\sigma$ , which is the distance where the Lenard-Jones potential reaches its minimum, leading to purely repulsive potentials (known as the Weeks-Chandler-Andersen potential[52]). Temperatures and pressures are reported in terms of the usual reduced units,  $T^* = Tk_B/\varepsilon$ , where  $k_B$  is Boltzmann’s constant, and pressure,  $P^* = P\sigma^3/\varepsilon$ .

Table 1 CSLJ used for each non-bonded potential

$\varepsilon_{AB}, C_{AB}$	Type 1	Type 2	Type 3
Type 1	$\varepsilon, 2\sigma$	$\varepsilon, 2^{1/6}\sigma$	$\varepsilon, 2^{1/6}\sigma$
Type 2	$\varepsilon, 2^{1/6}\sigma$	$\varepsilon, 2^{1/6}\sigma$	$\varepsilon, 2^{1/6}\sigma$
Type 3	$\varepsilon, 2^{1/6}\sigma$	$\varepsilon, 2^{1/6}\sigma$	$\varepsilon/2, 2\sigma$

Our model does not provide a specific mapping between each bead and a particular group of atoms, and it does not explicitly discriminate between alkane and perfluoro-alkane segments in the lateral chains. To get a precise atomistic-coarse grained mapping, some selected physical properties (*e.g.*, radial distribution functions, densities, *etc.*) calculated from simulations would need to be matched. While coarse-graining techniques exist that can accomplish such mapping for specific TBA chemistries[53-55], our model is intended to be generic and to capture the approximate behavior of molecules (of potentially different chemistries) that can roughly match the molecular

structure shown in Figure 2. Hence, our simple model is more suitable to provide a proof-of-concept of possible phase behavior than to provide specific predictions[48]. The previous work by Crane *et al.*[48] have already proved that this type of minimalistic model was able to capture the “crucial” characteristics of TBAs with a linear lateral chain to allow reproducing the experimentally observed complex mesophase behavior. In principle, introducing perfluoro-alkane segments into the lateral chain as in the molecule of Figure 1 (which would appear as a fourth type of bead in our model) can influence the mesophase behavior of the TBAs. Nevertheless, these perfluoro-alkane segments are expected to experience rather similar interactions as those of alkane segments and hence may not play a “critical” role in the mesophase behavior, at least compared with the stronger interactions between the other segment types (*e.g.*, the repulsive cores and the hydrogen bonds). Therefore, for the case of TBAs with a swallow-tail lateral chain, we use the same force field for all side-chain segments, and only consider differences in the shape of the lateral chain.

In our simulations, the rigid unit of the TBAs (encompassing bead types 1 and 2) is always the same while the lateral chain is systematically varied by increasing its number of beads. Accordingly, the chemical composition of the TBAs is characterized by the volume fraction of flexible lateral chains defined as

$$\phi_{\text{flx}} = \frac{V_{\text{flx}}}{V_{\text{mol}}} = \frac{V_{\text{flx}}}{V_{\text{flx}} + V_{\text{rigid}}} \quad (5)$$

where  $V_{\text{mol}}$  is the volume of one TBA molecule,  $V_{\text{flx}}$  is the volume of its lateral chain, and  $V_{\text{rigid}}$  is the volume of its rigid unit. Since it is non-trivial to define the volume of a “soft” molecule that adopts multiple conformations, an approximation[48] is made,

which assumes the rigid unit has spherocylindrical geometry and treats each bead in the lateral chain as a separate sphere. The volume of a molecule can thus be found below in terms of  $\sigma$

$$V_{\text{mol}} = V_{\text{rigid}} + V_{\text{flx}} = \left( 5 \times \frac{\pi \sigma^2}{4} \times 0.7 + \frac{\pi \sigma^3}{6} \right) + \left( N_{\text{flx}} \times \frac{\pi \sigma^3}{6} \right) \quad (6)$$

The density of LC phases is sometimes reported in experiments with the estimated packing fraction of the mesogenic molecules. Correspondingly, our system density is described by the packing fraction found from

$$\eta = \frac{V_{\text{mol}} N}{V_{\text{box}}} \quad (7)$$

where  $V_{\text{box}}$  is the volume of the simulation box, and  $N$  is the number of molecules in the simulation system. In our simulation,  $\eta$  was 0.45, corresponding to the number density about 0.85, which is a dense fluid phase for the Weeks-Chandler-Andersen potential[56]. Simulations were performed in continuum space *via* the LAMMPS molecular dynamics (MD) simulation package using cubic boxes and periodic boundary conditions[57]. VMD was used for visualization[58]. Simulations entailed the Micro-Canonical ( $NVE$ ) ensemble, and the Canonical ( $NVT$ ) ensemble. The actual fluids were expected to be nearly incompressible (*i.e.*, to have a smaller isothermal compressibility than that of the simulated models), so that the pressure was expected to have little impact on the actual phases observed over a wide range of pressures. Thus, most of the simulations were carried out using the  $NVT$  ensemble to keep the packing fraction,  $\eta$ , to be 0.45. For any system, the simulations were started at a higher temperature to reach first a well-equilibrated isotropic state. The system was then gradually cooled down by a temperature decrement of  $\Delta T^* = 0.05$  to allow molecules to spontaneously form

different LC phases. For each simulation run, we first decreased the temperature by  $\Delta T^* = 0.05$  over a period of  $t^* = 7500$ , and then equilibrated the system at the new temperature in a simulation time of  $t^* = 75000$ . The final configuration of the equilibration part was used as input for the next simulation run at a lower temperature. We collected configurations from the equilibration part for each temperature to analyze the phase morphology. An integration step size of  $\Delta t^* = 0.005$  was used for all simulations. Based on our observations, the system usually exhibits the isotropic state for  $T^* \geq 2.0$ , while it presents noticeable cavities for  $T^* \leq 0.30$ , indicative that, at very low temperatures, the assumption of fixed density breaks down as a strong preference for the system to pack more densely ( $>0.45$ ) leads to tension. Since characterizing solid-state behavior is beyond the scope of this work and our TBA molecules approach solid or glassy states at very low temperatures, our simulations were restricted to the  $0.30 \leq T^* \leq 2.0$  range.

It is important to emphasize that finite size effects can have a significant effect on the stability of some phases. The lamella and columnar phases which typically only possess 1D and 2D periodicity, respectively, are largely insensitive to the simulation box size since their morphologies can easily rotate in space to fit inside the simulation box. On the contrary, phases with 3D-periodic morphologies are sensitive to the box size as the box length needs to be a multiple integer of the unit cell size (which is not known *a priori*). At the same thermodynamic conditions, an inappropriate box size may frustrate the appearance of a 3D-periodic phase and lead instead to the appearance of metastable phases. Thus, simulations on multiple box sizes were performed to target the unit cell

size of 3D-periodic phases and to test the relative stability of any competing phase formed.

## **2.2 Analysis methods for 2D columnar phases**

To identify the columnar phases composed of honeycombed cylinders, we calculate several order parameters from the simulation configurations. These parameters allow a more quantitative description of the structure of LC phases, and the detection of phase transition points. For our model, it is convenient to define the direction (orientation vector) of each bolaamphiphile molecule as the axis of its rigid unit, which generate a set of unit vectors,  $\{\mathbf{u}_1, \mathbf{u}_2, \dots, \mathbf{u}_N\}$ , representing every molecule in the system.

**2.2.1 Lamella/Columnar director.** For lamella/columnar phases, the director (the order direction) may be viewed as the vector orthogonal to their layers, and is defined as a unit vector,  $\mathbf{n}$ , that is maximally orthogonal to the set of molecular orientation vectors. Concisely, this may be written as

$$\min(\|\mathbf{U}\mathbf{n}\|) \text{ subject to } \|\mathbf{n}\| = 1$$

where  $\mathbf{U}$  represent the  $N$  by 3 matrix containing all molecular orientation vectors,  $\mathbf{u}_i$ . The solution to this problem is obtained through determining the singular value decomposition (SVD) factorization of matrix  $\mathbf{U}$ , and the director,  $\mathbf{n}$ , found as the right singular vector of  $\mathbf{U}$  corresponding to the smallest singular value. Knowing the director, other order parameters can be calculated to quantify these 2D phases as described below.

**2.2.2 The planar order parameter.** The planar order parameter,  $S_2$ , measures how orthogonal the molecular orientation vectors are to the director vector, and is defined by

$$S_2 = \frac{\sum_{j=1}^N (3\sin^2\phi_j - 2)}{N} \quad (8)$$

where  $\phi_j$  is the angle between the director,  $\mathbf{n}$ , and the orientation vector of the  $j^{\text{th}}$  molecule. For an isotropic system where there is no correlation between the director and the orientation vector, the value of  $\phi_j$  ranges from  $0^\circ$  to  $180^\circ$ , and  $S_2$  approaches a value of 0. Conversely, for an ordered system where all the molecular orientation vectors lie on a plane orthogonal to the director, the values of  $\phi_j$  are concentrated around  $90^\circ$ , and  $S_2$  approaches a value of 1.

**2.2.3 The planar orientational order parameter.** To describe the geometry of the honeycombed cylinders (*i.e.*, to determine whether the columns are triangular/square/hexagonal), the planar orientational order parameter,  $\psi_k$ , is found from

$$\psi_k = \left| \frac{1}{N} \sum_{j=1}^N \exp(ik\theta_j) \right| \quad (9)$$

where  $\theta_j$  is the angle describing the polygonal symmetry of the column cross section. To find  $\theta_j$ , we need to define a plane,  $\mathbf{P}$ , which is orthogonal to the director,  $\mathbf{n}$ , and choose an arbitrary unit vector,  $\mathbf{n}'$ , on this plane. Then every molecular orientational vector,  $\mathbf{u}_j$ , is projected onto the plane,  $\mathbf{P}$ , as the projection vector  $\mathbf{u}'_j$ , which allows us to find a new set of molecular projection vectors,  $\{\mathbf{u}'_1, \mathbf{u}'_2, \dots, \mathbf{u}'_N\}$ .  $\theta_j$  is defined as the angle between  $\mathbf{n}'$  and the molecular projection vector of the  $j^{\text{th}}$  molecule,  $\mathbf{u}'_j$ . The coefficient  $k$  takes on the value of 2, 3, 4 and 6 for the lamella, triangular, square and hexagonal planar orientational order parameter, respectively. Similar to  $S_2$ , a  $\psi_k$  value close to 0 indicates a low level of order, while a  $\psi_k$  value close to 1 indicates a high level of order.

### 2.3 Analysis methods for 3D periodic order phases

Unlike the columnar phases, there is no convenient scalar order parameter that can unambiguously describe bicontinuous cubic phases. However, the specific geometry and topology of these phases provide a basis for their detection. Indeed, both the interwoven networks possess unique space group symmetries, and the remaining continuous phase shares features of some periodic minimal surfaces. The networks consist of struts connecting nodes, with the nodal valence ( $\nu$ )[37] being a key descriptor of different bicontinuous phases. The three different bicontinuous phases that are relevant for our systems are the double gyroid phases with  $\nu = 3$ ,  $Ia\bar{3}d$  symmetry and Schoen's gyroid minimal surface, the double diamond phases with  $\nu = 4$ ,  $Pn\bar{3}m$  symmetry and Schwarz's D-surface, and "plumber's nightmare" phases with  $\nu = 6$ ,  $Im\bar{3}m$  symmetry and Schwarz's P-surface[37].

The unique space group symmetry of different types of bicontinuous phases can be identified using the structure factor,  $S(\mathbf{q})$ , by applying Eq. (10)[59] to the component-forming networks (usually the rigid units in our system),

$$S(\vec{q}) = \frac{(\sum_j \cos(\vec{q} \cdot \vec{r}_j))^2 + (\sum_j \sin(\vec{q} \cdot \vec{r}_j))^2}{N} \quad (10)$$

where  $\mathbf{q}$  is the wave vector, the  $\mathbf{r}_j$ 's are the position vectors of the beads forming the networks, and  $N$  is the number of such beads. The wave vector,  $\mathbf{q}$ , is restricted to integer numbers of wavelengths within the simulation box, namely,  $\vec{q} = 2\pi(\frac{n_x}{L_x}, \frac{n_y}{L_y}, \frac{n_z}{L_z})$ . The location of peaks given by  $m = \sqrt{n_x^2 + n_y^2 + n_z^2}$ , are distinctive of different space group symmetries. The location of the peaks for the relevant bicontinuous phases have the

following ratios: ( $\sqrt{6}$ :  $\sqrt{8}$ :  $\sqrt{14}$ :  $\sqrt{16}$ :  $\sqrt{20}$ :  $\sqrt{22}$ ...) for the  $Ia\bar{3}d$  double gyroid, ( $\sqrt{2}$ :  $\sqrt{3}$ :  $\sqrt{4}$ :  $\sqrt{6}$ :  $\sqrt{8}$ :  $\sqrt{9}$ ...) for the  $Pn\bar{3}m$  double diamond, and ( $\sqrt{2}$ :  $\sqrt{4}$ :  $\sqrt{6}$ :  $\sqrt{8}$ :  $\sqrt{10}$ :  $\sqrt{12}$ ...) for the  $Im\bar{3}m$  plumber's nightmare phase[26]. The structure factor can also be used to detect the lamella phase (ratios 1: 2: 3: 4: 5: 6) and the hexagonal cylinder phase (ratios 1:  $\sqrt{3}$ :  $\sqrt{4}$ :  $\sqrt{7}$ :  $\sqrt{9}$ :  $\sqrt{12}$ ...)[26]. In addition, calculating  $S(\mathbf{q})$  can give an approximate estimate of the length of the unit cell " $L_{\text{ucell}}$ " of periodic structures[50] based on the location of the first refraction peak in  $S(\mathbf{q})$ , by applying Eq. (11)

$$L_{\text{ucell}} = \frac{2\pi}{q^*} m \quad (11)$$

where  $q^*$  is the modulus of the wave vector at which the maximum of  $S(\mathbf{q})$  is located, and  $m$  is the first spacing ratio for a particular periodic structure (e.g.  $m = 1$  for the lamellae and the hexagonal cylinder,  $m = \sqrt{2}$  for the double diamond and the plumber's nightmare phase, and  $m = \sqrt{6}$  for the gyroid)[50].

In our simulations, some cocontinuous phases with 3D periodicity are also observed, where one component forms a single network of struts connected by nodes. To form these networks, several rigid rods of the TBAs are bundled together becoming struts, and several struts merge into one node stabilized by the strong attraction among type 1 beads (which are connected at the ends of each rigid rod). Each strut can merge into two nodes at both ends. Hence, each node is a group of type 1 beads, and each strut is a group of type 2 beads (which form the inner sections of the rigid rods).

The characterization of these "single" network phases is usually done through simple visual inspection of simulation snapshots and calculating  $S(\mathbf{q})$ . To identify these cocontinuous phases quickly and qualitatively sketch their structure, here we propose a

method based on constructing the “skeleton” of the network where points represent each node and lines represent each strut (providing additional details in the Appendix). The topology of the resulting skeleton can then be analyzed to determine, *e.g.*, the nodal valence ( $v$ ), the total number of nodes in the simulation box ( $N_{\text{node}}$ ), the number of rigid rods in each strut ( $N_{\text{rod-strut}}$ ).

#### 2.4 The mobility coefficient

To quantify the mobility of TBA molecules in the different phases, the mean-squared bead displacement MSD is calculated using configurations collected from the *NVE* ensemble. The final configuration of *NVT* simulations at different temperature was used as input configuration of *NVE* simulations. Each *NVE* simulation was equilibrated for a simulation time of  $t^* = 2500$ , then configurations were collected at time intervals of  $\Delta\tau = 20$ , for a further production period of  $t^* = 10000$ . Assuming that the total number of timesteps (also the total number of configurations we collected) in the simulation is  $t$ , then for a given step size of timesteps,  $s$ , its corresponding MSD was calculated using the equation

$$R_s = \frac{\sum_{j=1}^{N(6+N_{\text{flx}})} \sum_{i=0}^{t-s} |\Delta r_{i+s,i}^j|^2}{N(6 + N_{\text{flx}})(t - s)} \quad (12)$$

where  $\Delta r_{i+s,i}^j$  is the displacement of the  $j^{\text{th}}$  beads in the system, between timestep  $i$  and  $(i+s)$ . A series of MSD values were calculated for different number of timesteps,  $s$ . The number of timesteps,  $s$ , was then converted into the reduced time,  $s\Delta\tau$ , where  $\Delta\tau$  is the size of each timestep. Since there is no direct calibration between the reduced time and the real time in the coarse-graining model, the diffusion coefficient of the system cannot

be simply calculated by the rate of change of the mean-squared displacement with time. Instead, the mobility coefficient ( $\mu$ ) is defined as this rate of change, which is still helpful to compare the relative mobility of different phases. Note that there are typically two distinct regimes in the plot of MSD vs. time. In the short-time regime, the MSD mainly reflects localized vibrations of the beads, and it typically exhibits a steep increase in the plot. In the long-time regime, the MSD mainly reflects non-local diffusive and hopping motions. These two regions are clearly delineated at low temperatures but become less indistinct at high temperature due to rapid non-local movements dominating over any localized vibrations. Since non-local motions were of primary interest, the mobility coefficient is obtained from the slope of the MSD in the longer time regime. As is seen from the Eqn. (12), larger values of the time interval  $s$  imply fewer sampling data in the averaging procedure, and hence less accurate MSD values. Therefore, linear regression of MSD data for an intermediate range of times was used to obtain the mobility coefficient.

## CHAPTER 3

### RESULTS

#### ***3.1 Global phase diagram***

A series of simulations were performed for different lengths of the lateral chain ( $3 \leq N_{\text{flx}} \leq 33$ ). A global phase diagram in terms of reduced temperature and volume fraction of the lateral chain ( $\phi_{\text{flx}}$ ) is presented in Figure 3. As can be seen from this figure, we obtained several morphologies including the lamella (L), polygonal columns, axial-bundle column, the double gyroid (G) and cocontinuous networks (*e.g.*, the “single” plumber’s nightmare (P1) and the “single” diamond (D1)). Some examples of the morphologies encountered in our simulation are shown in Figure 4. Note that the polygonal columnar phases and the axial-bundle columnar phases have the “inverse” domain topology. In the polygonal columnar phases, the rigid rods form a continuum domain to delineate the shell of each cylinder, and the lateral chains fill the inside of each cylinder. The rigid rods are perpendicular to the cylinder they formed. In the axial-bundle columnar phases, the rigid rods are bundled together to form isolated cylinders, which are separated by the continuum domain of the lateral chain, and the rigid rods are parallel to the cylinder. Compared with the experimental results shown in Figure 1, we obtained the same G phase formed by the rigid rods for  $0.752 \leq \phi_{\text{flx}} \leq 0.823$ , whereas experiments found the G phase at the lower range of  $0.726 \leq \phi_{\text{flx}} \leq 0.75$ . In the experiments, the axial-bundle columnar phase was found at the same  $\phi_{\text{flx}}$  as the G phase but at a different temperature, while we detected this columnar phase for  $\phi_{\text{flx}} = 0.841$ , where the G phase was not detected in simulations. In the experiments the double

diamond phase was observed for  $\phi_{flx} = 0.641$ , whereas our simulations failed to detect this phase. Instead, the D1 phase was found in the range  $0.638 \leq \phi_{flx} \leq 0.675$ . Details about each observed phase are discussed in the following sections.

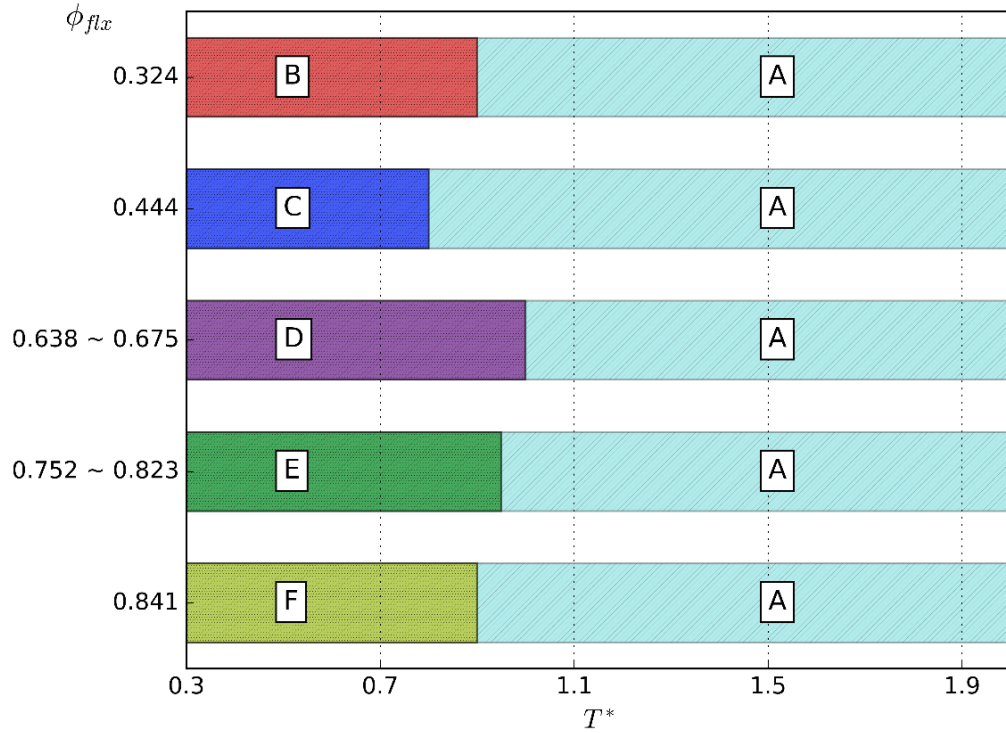


Figure 3 Morphologies obtained from simulations of TBAs with a swallow-tail lateral chain with the respect to temperature and volume fraction of the lateral chain. Morphology description: (A) isotropic; (B) square column; (C) “single” plumber’s nightmare network; (D) “single” diamond network; (E) double gyroid; (F) axial-bundle columns.

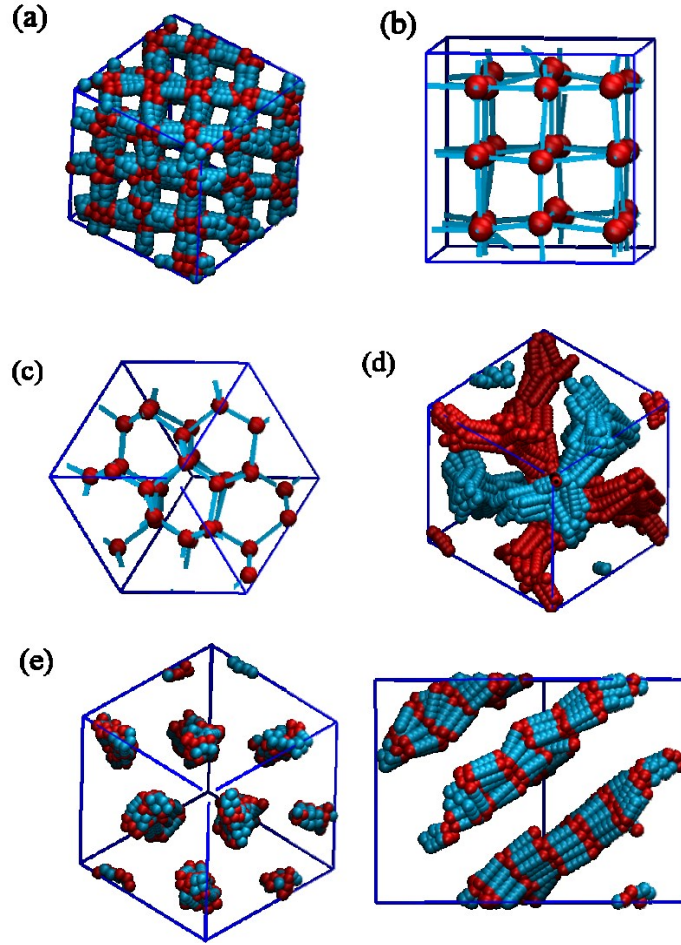


Figure 4 Sample snapshots of equilibrium configurations of TBAs with a swallow-tail lateral chain. For clarity, only the rigid rods are shown, and only the skeleton of the network is shown in (b) and (c). For (a) (b) (c) (e), the type 1 beads are colored red, the type 2 beads are colored blue. For (d), two distinct networks, which never intersect, are colored red and blue, respectively. From (a) to (e), the phases correspond to  $N_{\text{flx}} = 3, 5, 11, 19, 33$  and  $\phi_{\text{flx}} = 0.324, 0.444, 0.638, 0.752, 0.841$ , respectively.

### 3.2 2D and 3D periodic phases

**3.2.1  $N_{\text{flx}} = 3$ .** In this case, the corresponding volume fraction is about  $\phi_{\text{flx}} = 0.324$ , and a square columnar phase is obtained (see Figure 4(a)). This square columnar structure exists for a temperature range of  $T^* \leq 0.90$ , which is confirmed by the order parameters  $S_2$  and  $\psi_4$  (Figure 5). Around  $T^* = 0.90$ ,  $S_2$  exhibits a steep increase from

0.11 to 0.76, while  $\psi_4$  also shows an increase from 0.06 to 0.50, indicating a phase transition from an isotropic state to a square columnar structure. With a further decrease of temperature, the value of  $S_2$  and  $\psi_4$  increases gradually, reaching values of 0.95 and 0.82 at  $T^* = 0.30$ , respectively.

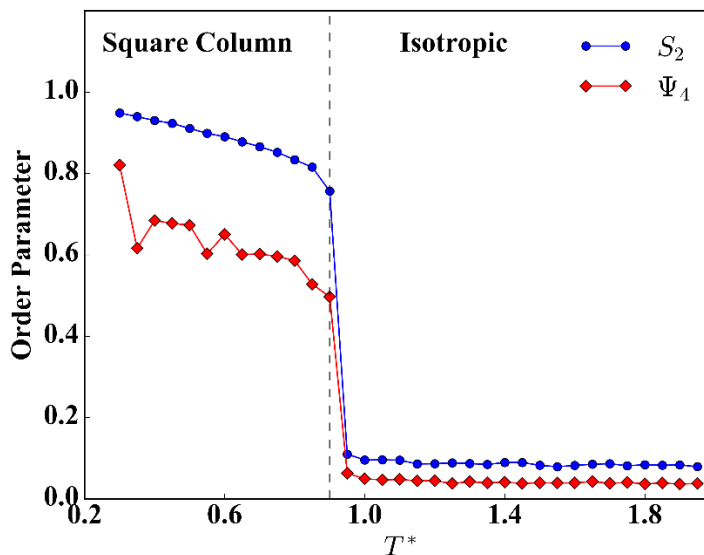


Figure 5 Order parameters for the TBAs with  $N_{\text{fix}} = 3$  as a function of temperature.

**3.2.2  $N_{\text{fix}} = 5$  ( $\phi_{\text{fix}} = 0.444$ ).** These molecules form a cocontinuous phase with 3D periodicity corresponding to the “single” plumber’s nightmare (P1) phase (see Figure 4(b)) between  $T^* = 0.30$  and  $T^* = 0.85$ . Lack of a single scalar order parameter to characterize this P1 phase, we are only able to roughly determine its temperature range of stability through inspecting simulation snapshots and calculating the structure factor. Ideally, the rigid rods in the P1 phase would form a single network of struts connected by 6-fold nodes, and the nodal valence ( $v$ ) be exactly 6. Upon calculation of the network skeleton at  $T^* < 0.85$  (Figure 6) as described in Section 2.3, we find there are some defects in our simulated structures. The nodal valence ( $v$ ) population distribution (see Figure S1(a) in the Appendix) shows that some nodes have  $v < 6$ , indicating that some

struts connecting neighbor nodes are missing. Also, some nodes have  $v > 6$ , indicating that some struts connect two nodes which are not nearest neighbors. Although there is no reported information about the structure factor ( $S(\mathbf{q})$ ) of the P1 phase, the nodes in this phase have a symmetry similar to that of the simple cubic (SC) crystal structure. Therefore, the  $S(\mathbf{q})$  of SC (ratios  $1: \sqrt{2}: \sqrt{3}: \sqrt{4}: \sqrt{5}\dots$ ) can help us detect the P1 phase and calculate its unit cell size. As mentioned in Section 2.3, each node in the networks is a cluster of type 1 beads. To match the results of SC, only the position vectors of the beads forming the nodes (which is type 1 beads) are used to calculate the structure factor. The location of the peaks of  $S(\mathbf{q})$  shows good agreement with the expected ratios of a SC structure (see Figure 7), which, along with the network-skeleton analysis, confirms the “single” plumber’s nightmare symmetry of this phase.

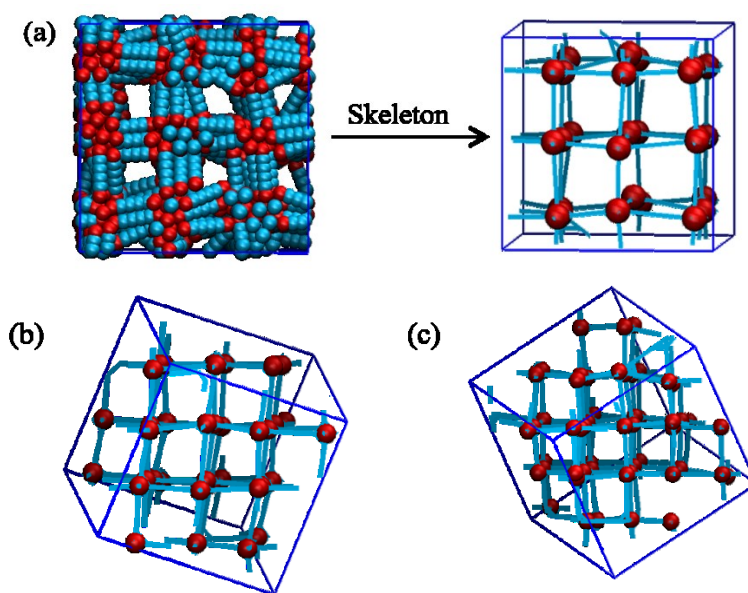


Figure 6 Snapshots of the P1 phase and its corresponding skeleton for different box sizes. For clarity, only the rigid rods are shown. Red spheres represent the type 1 beads, and blue spheres represent the type 2 beads. (a)  $L_{\text{box}} = 17.36$  and  $N = 400$  molecules; (b)  $L_{\text{box}} = 19.88$  and  $N = 600$  molecules; (c)  $L_{\text{box}} = 21.88$  and  $N = 800$  molecules.

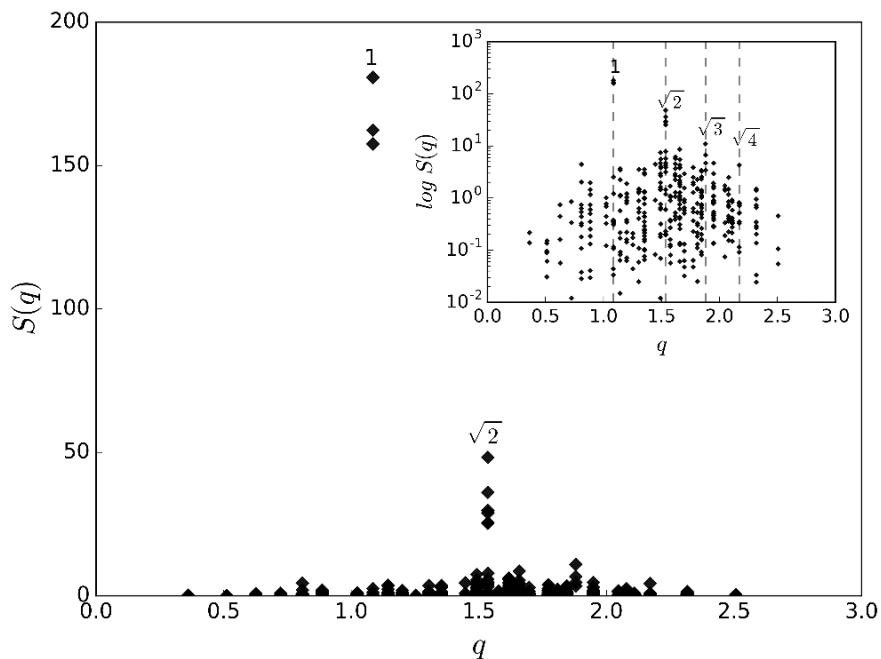


Figure 7 Structure factor calculated from a simulated snapshot of the P1 phase for TBAs with  $N_{\text{flx}} = 5$  and  $N = 600$ . The inset shows the structure factor on a logarithmic scale.

Due to the potential importance of finite size effects in the stability of 3D morphologies, multiple box sizes were performed to target the unit cell size and test the stability of the P1 phases. Three box sizes ( $L_{\text{box}} = 17.36, 19.88, 21.88$ ) were chosen, corresponding to  $N = 400, 600, 800$  molecules. We repeated the simulations three times for  $N = 400$ , and only ran simulations once for  $N = 600$  and  $800$ . The P1 phase was observed for all the three box sizes, and no alternative morphologies were observed (see Figure 6), indicating that this phase is not very sensitive to box size.  $S(q)$  was used to help us determine the unit cell size ( $L_{\text{ucell}}$ ) using Eq. (11) (with  $m = 1$ ), and the network-skeleton analysis was used to characterize the network composition (*i.e.*, via  $N_{\text{node}}$  and  $N_{\text{rod-strut}}$ ). We also calculated  $N / N_{\text{node}}$  to provide a relative scale for the network composition. These results are summarized in Table 2, and show slight discrepancies for different box sizes, likely correlated to the different orientation that this P1 phase

needs to adopt to fit into the different boxes. The  $L_{\text{ucell}}$  of the P1 phase turns out to be small (around 5.79 ~ 5.99), which means that the box sizes we used can accommodate several multiples of the unit cell, making the finite size effects relatively small. The skeleton-network calculation confirms that each strut in the network consists of one bundles of rigid rods, and each bundle contains about 5.13 ~ 5.52 rigid rods on average.

Table 2 Average properties of the P1 phase for different box sizes.  $N$  is the number of molecules in the simulation box;  $L_{\text{box}}$  is the length of the simulation box;  $L_{\text{ucell}}$  is the length of the calculated unit cell;  $N_{\text{node}}$  is the number of nodes of the network in the box;  $N_{\text{rod-strut}}$  is the average number of rigid rods in a strut of the network.

$N$	$L_{\text{box}}$	$L_{\text{ucell}}$	$N_{\text{node}}$	$N / N_{\text{node}}$	$N_{\text{rod-strut}}$
400	17.36	5.79	26.45	15.12	5.13
600	19.88	5.99	35.40	16.95	5.52
800	21.88	5.85	51.45	15.55	5.24

The information collected from the mobility coefficient  $\mu$  (see Figure 8) allow us to further characterize the P1 phase. For  $T^* \leq 0.45$ , the value of  $\mu$  is close to zero, suggesting a solid crystalline phase. For  $T^* > 0.45$ ,  $\mu$  increases linearly with temperature until its transition to an isotropic phase at  $T^* = 0.85$ . The finite values of  $\mu$  in this region suggest these ordered phases have some fluidity consistent with a LC character. For instance, inspection of simulation snapshots for the P1 phase at  $T^* = 0.60$  reveals that the rigid rods bundled together into struts are not restricted to local vibration around one specific strut, but some of the rods can hop from one strut to another (see the supplementary material P1.avi). At  $T^* = 0.85$ , there is a large increase in  $\mu$  associated

with the transition to an isotropic phase, followed by a linear increase of  $\mu$  with temperature.

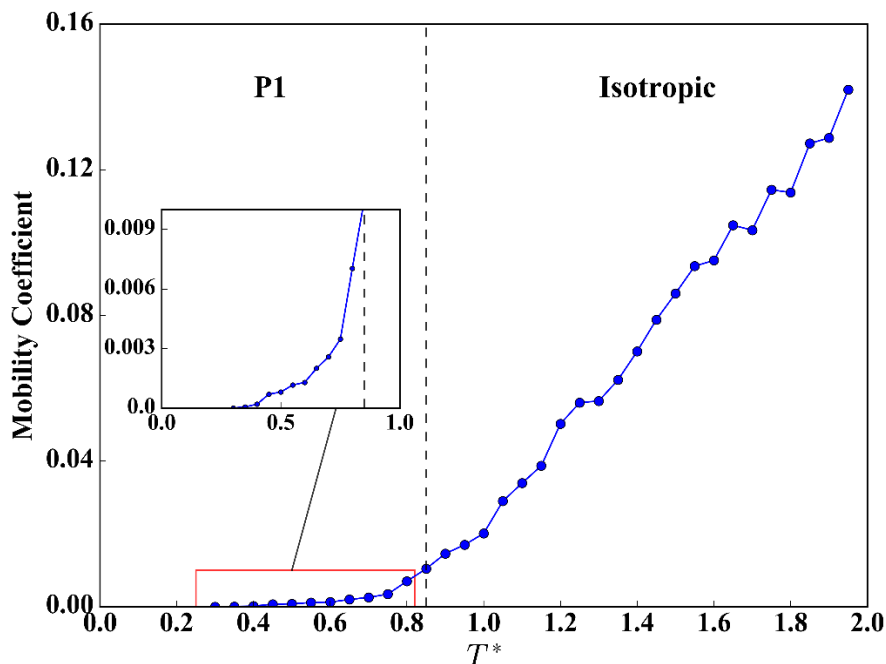


Figure 8 The mobility coefficient for  $N_{\text{fix}} = 5$  TBAs with  $N = 600$  as a function of temperature. “P1” refers to the morphology of the “single” plumber’s nightmare phase.

**3.2.3  $N_{\text{fix}} = 7, 9$ .** For molecules with  $N_{\text{fix}} = 7$ , corresponding to  $\phi_{\text{fix}} = 0.528$ , only cocontinuous phases without periodicity are observed for  $T^* \leq 1.0$ . The network-skeleton analysis provides some characterization of the topology of these disordered network structures. The nodal valence ( $v$ ) population distribution (Figure S1(b)) shows that a large proportion of nodes have  $v$  values of 4, 5 and 6, indicating an intermediate structure between the P1 network ( $v = 6$ ) and the D1 network ( $v = 4$ ). As for molecules with  $N_{\text{fix}} = 9$ , corresponding to  $\phi_{\text{fix}} = 0.590$ , only the defective D1 phases are observed for  $T^* \leq 0.95$ . The  $v$  population distribution (Figure S1(c)) shows a large portion of

nodes have the  $v$  of 4. A small portion of nodes has the  $v$  of 3, 5, 6, which confirms the existence of defects in the network.

**3.2.4  $N_{\text{fix}} = 11, 13$ .** These cases map into volume fractions of 0.638 and 0.675, respectively. For  $0.3 \leq T^* \leq 1.0$ , we found a cocontinuous phase with 3D periodicity having the topology of a “single” diamond (D1) phase (see Figure 4(c)). As with  $N_{\text{fix}} = 5$ , the temperature range of stability of this D1 phase is determined through inspecting simulation snapshots and calculating structure factor. Through the network-skeleton analysis, we can easily determine the symmetry of the D1 phase, where bundled rigid rods form a single network of struts connected by 4-fold nodes. The nodal valence ( $v$ ) population distribution confirms the absence of defects in this diamond network, since all the nodes have the  $v$  of 4. The  $S(\mathbf{q})$  of the diamond cubic (DC) crystal structure (ratios  $\sqrt{3}: \sqrt{8}: \sqrt{11}: \sqrt{16} \dots$ ) provides a suitable reference to detect the D1 phase and calculate its unit cell size. Accordingly, the position vectors of the type 1 beads were used to calculate  $S(\mathbf{q})$  and found that the location of its peaks matches well with the ratios expected for the DC structure (see Figure 9), which, along with the network-skeleton analysis, confirms the “single” diamond symmetry of the network.

Multiple box sizes were simulated to target the unit cell size and test the stability of the D1 phases. Four box sizes were chosen, corresponding to  $N = 100, 400, 600, 800$  molecules. We repeated the simulations three times for  $N = 100$  and 600, and only ran simulations once for  $N = 400$  and 800. The D1 phase is observed for all the four box sizes, and no alternative morphologies were observed (see Figure S2), indicating that this phase is not very sensitive to the box size. The calculated unit cell size and the network composition (reported in Table S1) show slight discrepancies for different box

sizes, likely arising from the D1 phase trying to fit in the different boxes by rotation in space and slightly distorting its configuration. Note that for the case of  $N = 100$  molecules, the  $L_{\text{ucell}}$  given by the Eq. (11) coincides exactly with the simulation box edge. The small unit cell of the D1 phase (around 12.12 ~ 12.61) explains its low sensitivity to the relatively large simulation box sizes we used which are several times the size of the unit cell, thus making the finite size effects relatively small. Each strut in the network consists of one bundle of around 5.56 ~ 6.25 rigid rods, a structure that is close to that observed for the struts of the P1 phase (in Section 3.2.2). The number of rigid rods in a bundle is limited by the fact that the lateral chain of all molecules must have access to the internetwork continuous phase[45].

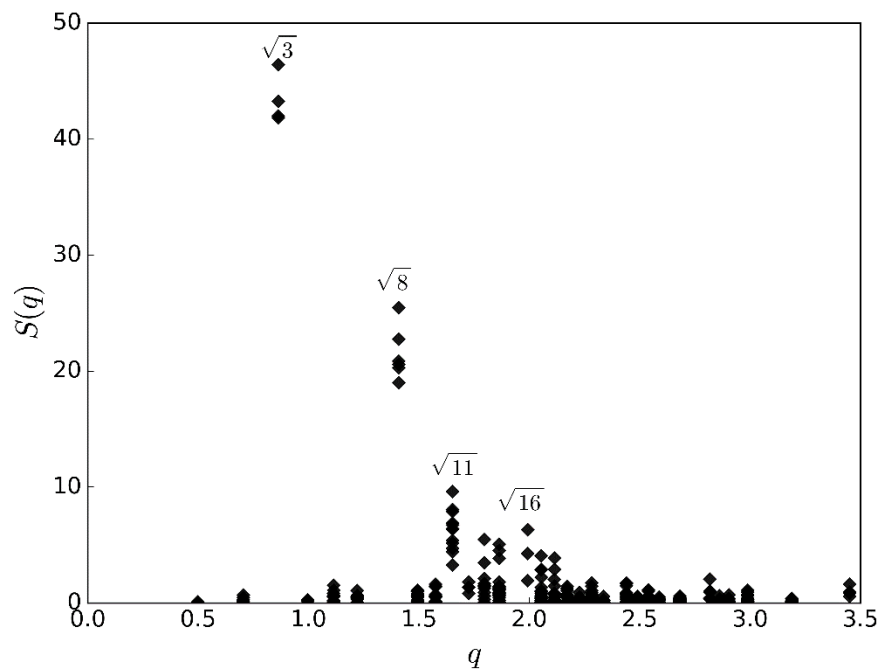


Figure 9 Structure factor calculated from simulated snapshot of the D1 phase for the  $N_{\text{fix}} = 11$  TBAs with  $N = 100$ .

As with  $N_{\text{flx}} = 5$ , further insight into the phase behavior of the system may be obtained by examining the variation of the mobility coefficient with temperature (see Figure S3). The results are consistent with three regimes, an isotropic phase for  $T^* > 1.0$ , an LC phase for  $0.5 < T^* < 1.0$ , and a solid crystalline phase for  $T^* < 0.5$ . Tracking of simulation snapshots in the LC region also reveal that the rigid rods in the D1 phase are not restricted to local vibration around one specific strut, but some of the rods can hop from one strut to another over longer time scales (see supplementary material D1.avi).

All the results discussed above were obtained for the same packing fraction,  $\eta = 0.45$ , but we also tested the stability of this D1 phase for different packing fraction. For  $\eta = 0.5$ , we found that the D1 phase is also stable for molecules with  $N_{\text{flx}} = 11$  and 13, and for  $T^* < 1.35$  (see Figure S5). By increasing the volume fraction, the ordered packing of the molecules is favored, which shifts the transition point between isotropic and LC phases to a higher temperature.

**3.2.5  $N_{\text{flx}} = 15, 17$ .** For these systems, only disordered cocontinuous phases without periodicity are observed for  $0.3 \leq T^* \leq 1.0$ . For example, for molecules with  $N_{\text{flx}} = 17$ , corresponding to  $\phi_{\text{flx}} = 0.731$ , the nodal valence ( $v$ ) population distribution (Figure S1(d)) shows a large portion of nodes have the  $v$  of 4 and 3, indicating an intermediate structure between the D1 phase ( $v = 4$ ) and the G phase ( $v = 3$ ).

**3.2.6  $N_{\text{flx}} = 19-29$ .** For a wide range of volume fraction ( $N_{\text{flx}} \sim 19-29$ , corresponding to  $0.752 \leq \phi_{\text{flx}} \leq 0.823$ ), the double gyroid (G) phase (see Figure 4(d)) is observed for  $0.3 \leq T^* \leq 0.95$ . Depending on the volume fraction of the lateral chain, this temperature range of G-phase stability varies slightly. In this G phase, the rigid rods form two interwoven networks of struts connected by 3-fold nodes, which is separated by a

continuous matrix of lateral chains. In our simulations, the G phase is obtained for the system of  $N = 300$  molecules, and the G phase is very stable at this condition. We repeated the simulations three times for each  $N_{\text{flx}}$  from  $19 \leq N_{\text{flx}} \leq 29$ , and only the G phase was observed. The details of these simulations are summarized in Table S1.2. The calculation of  $S(q)$  using the rigid rods (see Figure 10) confirms the G symmetry by the characteristic ratios of the location of the peaks with  $(\sqrt{6}: \sqrt{8}: \sqrt{14}: \sqrt{16}: \sqrt{20}: \sqrt{22})$ . Moreover, the size of the unit cell given by Eq. (11) coincides exactly with the simulation box edge (see Table S1.2). The network-skeleton analysis shows that there are 16 nodes and 24 struts in this G network for  $N = 300$ . Each strut in the network consists of 12.5 rigid rods forming two bundles, a structure that is close to that observed in the experiment (11.8 ~ 13.3 rigid rods)[44].

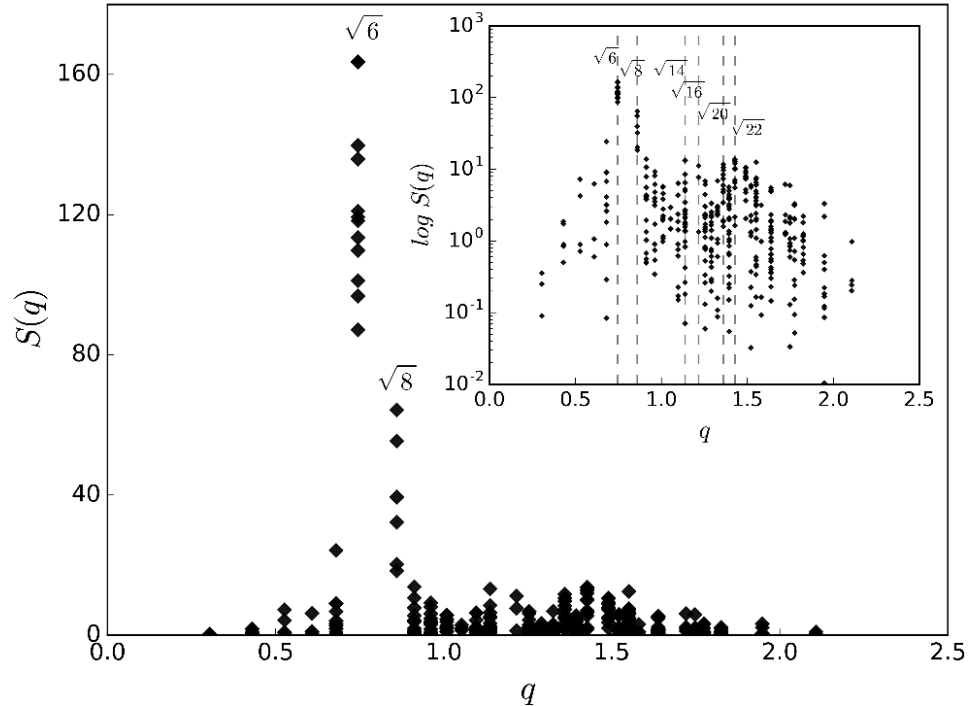


Figure 10 Structure factor calculated from a simulated snapshot of the G phase for  $N_{\text{flx}} = 19$  TBAs with  $N = 300$ . The inset shows the structure factor on a logarithmic scale.

Different morphologies of the nodes in the G phase were observed through the network-skeleton analysis. Ideally, the node in the G phase is the intersection of three struts, and is a cluster of type 1 beads (see Figure 11(a)). In the simulations, two non-ideal morphologies were identified. One case occurs when the node becomes a bundle of the rigid rods, and three struts merge into this bundle, where two struts are connected to its ends and one strut is connected to its body (see Figure 11(b), the non-ideal node is colored green and purple). The other case occurs when the node is represented by three bundles of the rigid rods, which connect to each other to form the triangular shape, and three struts are connected to the vertices of this “triangle” (see Figure 11(c), the non-ideal node is colored green and purple). In the latter case, the node is easily classified as three small nodes with  $v = 3$ . However, in the network-skeleton analysis, the correction of this misclassification is made, and the node with either non-ideal morphologies counts as one node with  $v = 3$ .

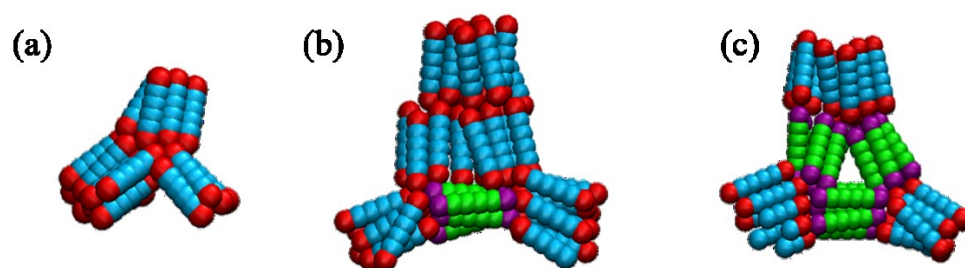


Figure 11 Sample snapshots of the different node morphologies in the G phase. The type 1 beads are colored red and purple, and the type 2 beads are colored blue and green.

Simulations for multiple box sizes were performed for molecules with  $N_{\text{fix}} = 19$ . Simulations for  $L_{\text{box}} = 19.94, 21.32, 22.74, 26.03$ , corresponding to  $N = 270, 330, 400, 600$  molecules, all failed to obtain the G phase, and only the disordered cocontinuous

phases were observed. Compared with the unit cell size calculated from the  $S(\mathbf{q})$  of the system of  $N = 300$  molecules, the simulation boxes used are around one unit. The finite size effects are relatively strong, and only the “correct” box size ( $L_{\text{box}} = L_{\text{ucell}}$ ) can form the G phase. Increasing the box size edge to be a multiple integer of the unit cell can, in principle, relieve any geometric frustration that arrests the formation of the G phase. However, due to the large unit cell size already, the dynamics of a large system slows down and equilibrating phases becomes increasingly difficult and expensive.

The results of the mobility coefficient (Figure S4) are consistent with the presence of 3 regimes corresponding to an isotropic phase for  $T^* > 1.05$ , an LC phase for  $0.60 < T^* < 1.05$ , and a solid crystalline phase for  $T^* < 0.60$ . Since the G phase structural signature is detected for  $T^* \leq 0.95$ , it suggests that the LC-like mobility observed for  $0.95 < T^* < 1.05$  would signal the presence of partially ordered LC morphologies (*i.e.*, consistent with either a gradual G-isotropic phase transition). We also tested the effect of packing fraction on the stability of the G phase and we find again that for a higher packing fraction,  $\eta = 0.5$ , the temperature range of G-phase stability is enhanced to  $T^* < 1.30$ , but the G phase only forms for molecules with  $N_{\text{flx}} = 19, 21, 23$  (see Figure S5).

**3.2.7  $N_{\text{flx}} = 33$ .** This is the TBA with the longest lateral chain that we considered, corresponding to  $\phi_{\text{flx}} = 0.841$ . The axial-bundle columnar phase (see Figure 4(e)) is found for  $0.3 \leq T^* \leq 0.90$ . In this case, the rigid rods are still bundled together, but due to the low volume fraction of rigid rods, these bundled rods cannot connect to each other to become a continuous network. Thus, these rods are separated into several isolated columns by a contiguous domain of lateral chains, and the columns arrange themselves into a hexagonal pattern. The calculation of  $S(\mathbf{q})$  using the rigid rods (see Figure 12)

confirms the hexagonal cylinder symmetry by the characteristic ratios of the location of the peaks with  $(1: \sqrt{3}: \sqrt{4})$ .

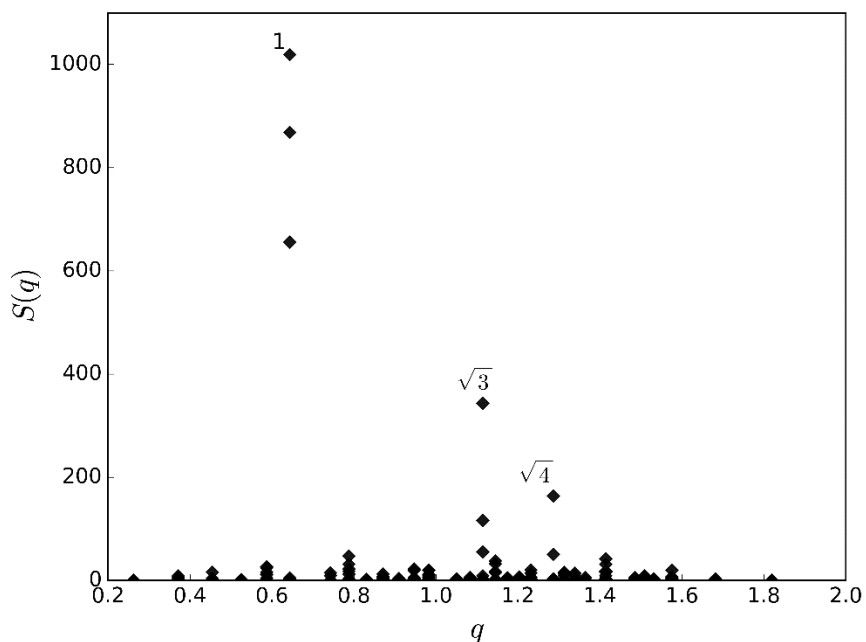


Figure 12 Structure factor calculated from a simulated snapshot of the hexagonal cylinder phase for  $N_{\text{flx}} = 33$  TBAs with  $N = 300$ .

### 3.3 Comparison of linear vs. swallow-tail TBAs

In mapping the phase behavior of the TBA with a swallow-tail lateral chain, it is also important to try to understand the relationship between the architecture of the molecules and the ordered phase they form. As mentioned before, Crane *et al.* simulated the phase behavior of the TBA with a linear lateral chain, and only found the polygonal columnar and lamella phases. We also performed some simulations for TBAs with a linear lateral chain at  $\eta = 0.45$ . Our simulation results confirm that, for the same  $N_{\text{flx}}$  and  $\phi_{\text{flx}}$ , arranging the lateral chain into different architectures (linear and swallow-tail) lead to the formation of different mesophase structures (see Figure S6). For example, for the

case of  $N_{\text{flx}} = 19$ , we find that TBAs with a linear lateral chain forms the lamella (L) phase for  $T^* \leq 1.20$ , while the TBA with a swallow-tail lateral chain forms the G phase for  $T^* \leq 0.95$ .

To understand the thermodynamic driving force behind these behaviors, we devised a simulation method (whose algorithmic details are provided in the Appendix) to allow the  $N_{\text{flx}} = 19$  TBAs with a swallow-tail lateral chain to form the L phase, and the molecule with a linear lateral chain to form the G phase. In this manner, we can investigate the energetic and entropic contributions to the free energy for the same lateral chain architecture but in different morphologies.

First, we compare the total potential energy,  $U_{\text{total}}$ . Table 3 shows the total potential energy for the TBAs in the L and G phase at  $T^* = 1.30$ . We note that, for the different molecular architectures, the  $U_{\text{total}}$  in the G phase is always more positive than the  $U_{\text{total}}$  in the L phase, indicating that TBAs show an energetic preference for the L phase over the G phase regardless of the molecular architecture.

Table 3 Total potential energy per bead ( $U_{\text{total}}$ , in units of  $\varepsilon$ ) of the TBA for three distinct structures.  $U_{\text{total}}(\text{swallow-tail})$  is for the TBA with a swallow-tail lateral chain;  $U_{\text{total}}(\text{linear})$  is for the TBA with a linear lateral chain;

	Gyroid	Lamella
$U_{\text{total}}(\text{swallow-tail})$	-0.442	-0.497
$U_{\text{total}}(\text{linear})$	-0.449	-0.516

Considering that the rigid rods and the 3 types of building blocks that make up a TBA are identical in both systems, the only difference is the architecture of the lateral chain (linear- and swallow-tail), indicating the precise topology of the lateral chain and its

associated conformational behavior may also have a profound effect on mesophase behavior. To study the conformational behavior of the lateral chain, the isotropic phase is chosen as our reference phase, since in this phase the lateral chains should be at their most relaxed, maximum conformational-entropy state (*i.e.*, unconstrained by the spatial confinement they are subjected inside mesophases). To characterize the conformational behavior of the lateral chains we examined their distribution of end-to-end distances  $R_{ee}$  (see also Figure S8).

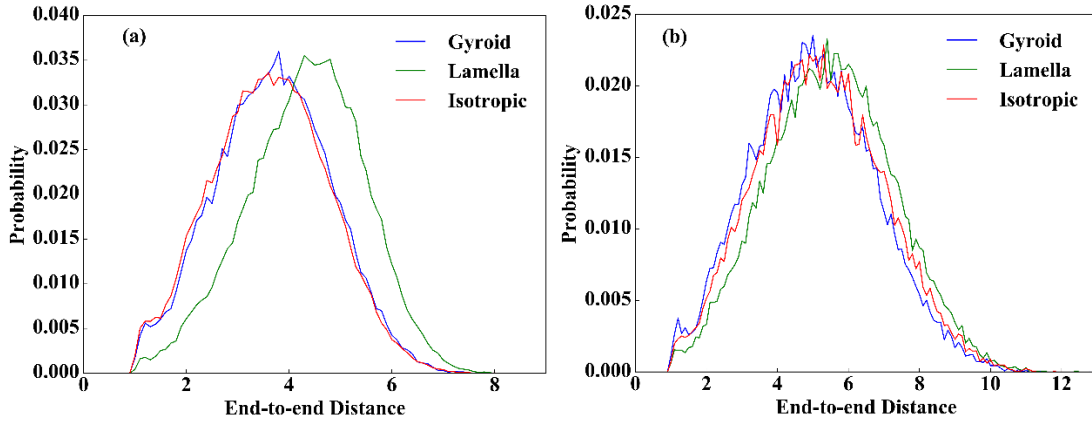


Figure 13 End-to-end distance for TBAs with  $N_{\text{fix}} = 19$ . (a) The TBA with a swallow-tail lateral chain in three distinct structures (isotropic, L and G); (b) The TBA with a linear lateral chain in three distinct structures.

Figure 13(a) shows these  $R_{ee}$  distributions for the swallow-tail lateral chain in the isotropic, L and G phase at  $T^* = 1.30$ . The  $R_{ee}$  distribution in the G phase is very close to that in the isotropic phase, while the distribution clearly shifts to higher values in the L phase. This indicates that, to form the lamella phase, the swallow-tail lateral chain needs to be significantly stretched, which would reduce the entropy of these chains and hence make the L phase to be less favorable than the G phase. Figure 13(b) shows the

$R_{ee}$  distribution found for TBAs with linear lateral chains at  $T^* = 1.30$ . Compared with the isotropic-phase  $R_{ee}$  distribution, the L-phase distribution slightly shifts to higher  $R_{ee}$  values, while the G-phase distribution slightly shifts to lower  $R_{ee}$  values. In this case, the collected information on  $R_{ee}$ 's indicates that the linear lateral chain TBA doesn't show a marked entropic preference for the L phase over the G phase.

In summary, for the linear lateral chain TBA, the L phase is more favorable than the G phase because the observed energetic preference would be determinant given that no marked entropic preference for either phase was detected. However, for the swallow-tail lateral chain TBA, the G phase is more favorable than the L phase because of the dominance of the entropic effect, which would more than compensate for the less favorable energetic interactions.

## CHAPTER 4

### CONCLUSIONS

Motivated by recent experimental findings involving bolaamphiphiles with a swallow-tail lateral chain[44,45], this simulation work explored the phase behavior of such molecules using a simple coarse-grained model. At a constant packing fraction of  $\eta = 0.45$ , different phases are observed depending on the length of the lateral chain, the temperature and the box size. The simulations were successful at detecting the double gyroid phase and the axial-bundle columnar phase, whose structures are similar to those of the corresponding phases found in recent experiment[44]. However, our simulations failed to detect the double diamond phase observed in recent experiment[45]. This failure may be related to the limitations of the coarse-grained model we adopted. This model may oversimplify some atomistic-level details, which would play a key role in the formation of the double diamond phase. Unexpectedly, the simulation predicts the formation of two regular cocontinuous phase with 3D-periodicity yet to be reported in experimental studies, including the “single” plumber’s nightmare phase P1 and the “single” diamond phase D1. As some of these novel phases may be amenable to experimental realization, our results may provide useful guidance for future efforts that employ such molecular designs.

The simple coarse-grained model used in this work can qualitatively capture some of the key physical features of the real TBA molecules, and hence reproduce most of the experimentally observed phases. However, simulations of more detailed, fully atomistic models are also important, especially to provide specific predictions for the TBA

chemistry, the local packing of atomic groups, and the thermophysical properties that will determine their value for potential applications, e.g., for creating self-assembled organic semiconductors for charge carrier transport. This study should hence be regarded as a first exploratory step toward modeling the phase behavior of TBAs. The relationship between the molecular architecture and phase behavior was not fully resolved by our study. Further studies employing free energy calculations will allow a more definitive determination of mesophase stability, especially where more than one phase is spontaneously formed by TBAs with linear or swallow-tail lateral chains. Such undertaking is non-trivial, especially for phases with 3D periodicity where free energies cannot be simply obtained by the use of molecular-insertion based method and require specialized thermodynamic integration schemes[60]. Work along these lines is currently under way.

## APPENDIX

### Network-skeleton analysis

As mentioned in the main text, we propose and implement a network-skeleton analysis to help us characterize the topology of any network that the rigid rods in the TBAs may be forming. In such a skeleton, points represent nodes and lines represent struts. In the coarse-grained model, each rigid rod consists of two type 1 beads and four type 2 beads. In the network, each node is a cluster of type 1 beads, and each strut is a cluster of type 2 beads (which also form the inner sections of the rigid rods). Here, we provide the main steps to perform this analysis:

1. Classify all the type 1 beads into different nodes. For each such bead  $i$ , we define its neighboring beads as the beads within the cutoff distance,  $d_c$ , chosen to be  $1.3\sigma$ . Based on the condition that any bead from a cluster can find all its neighboring beads in the same cluster, we classify the beads into different clusters, and each bead only belong to one cluster. Each cluster represents a node in the network. Hence, the number of such clusters represents the number of nodes in the network ( $N_{\text{node}}$ ).

2. Classify all the rigid rods into different struts. After step 1, the two type 1 beads from the same rigid rod must have been classified into two different nodes. Thus, for each rigid rod, we know which two nodes it connects. All the rigid rods, which merge into the same two nodes at their ends, are classified as one strut. After all rods have been sorted out, we collect the information of the number of rigid rods in each strut ( $N_{\text{rod-strut}}$ ).

3. Determine the neighboring nodes for each node classified in step 1. After step 2, we know which two nodes are connected by the same strut. Hence, any two nodes

connected by the same strut are treated as neighboring nodes. The number of the neighboring nodes of a given node in the network is the valence ( $\nu$ ) of that node.

4. Draw the skeleton of the network. Each node is represented by the center of mass of the type 1 beads belonging to the same node (as per the classification in step 1). Each strut is represented by a straight line connecting the two corresponding neighboring nodes (as per the information collected from step 3).

#### Additional data for simulations at $\eta = 0.45$

As indicated in the main text, most of our simulations were performed at a packing fraction of  $\eta = 0.45$ . The network skeleton analysis and the mobility coefficient are used to further characterize the structure and dynamics of different 3D-periodic phases that were observed. In this section, we provide additional data collected from the network skeleton and the mobility coefficient.

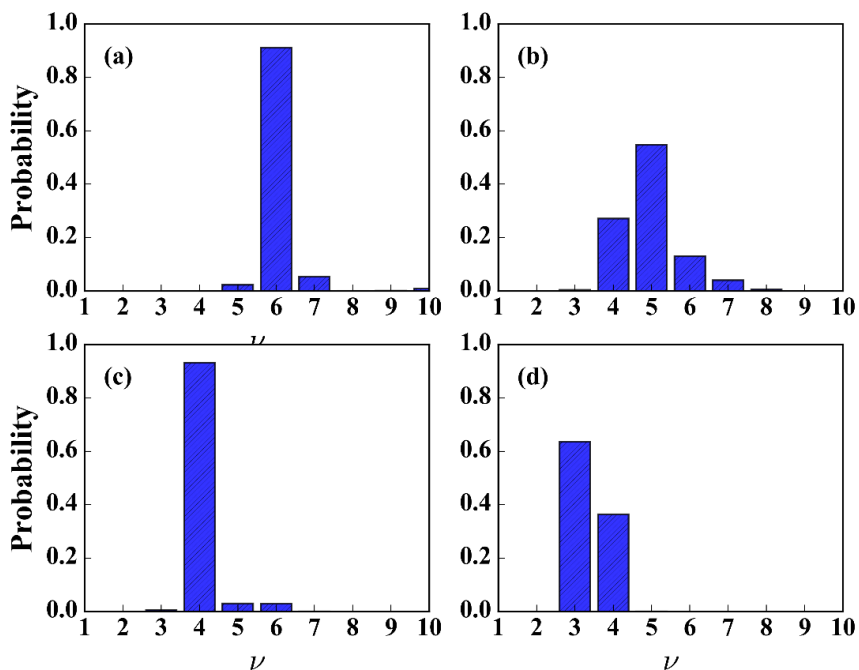


Figure S1 The population distribution of the nodal valence ( $\nu$ ) for molecules with different length of the lateral chain. (a)  $N_{fx} = 5$ ; (b)  $N_{fx} = 7$ ; (c)  $N_{fx} = 9$ ; (d)  $N_{fx} = 17$ .

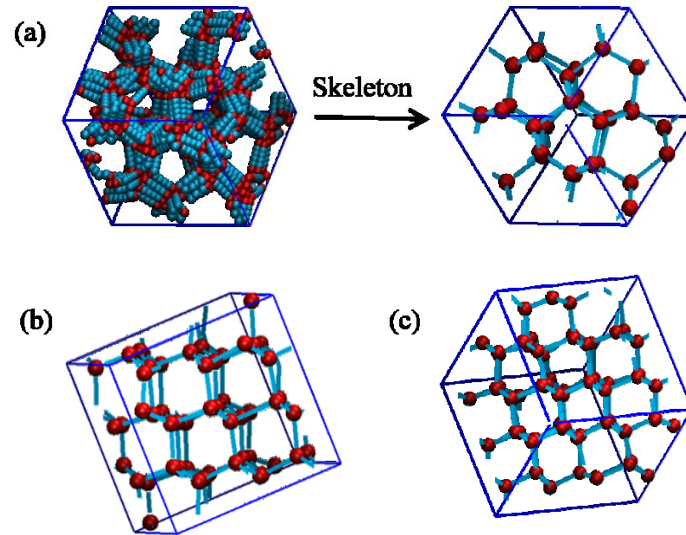


Figure S2 Snapshots of the D1 phase and its corresponding skeleton for different box sizes. For clarity, only the rigid rods are shown. Red spheres represent the type 1 beads, and blue spheres represent the type 2 beads. (a)  $L_{\text{box}} = 20.00$  and  $N = 400$  molecules; (b)  $L_{\text{box}} = 22.92$  and  $N = 600$  molecules; (c)  $L_{\text{box}} = 25.23$  and  $N = 800$  molecules.

Table S1 Average properties of the D phase network for different box sizes.  $N$  is the number of molecules in the simulation box;  $L_{\text{box}}$  is the length of the simulation box;  $L_{\text{ucell}}$  is the length of the calculated unit cell;  $N_{\text{node}}$  is the number of nodes of the network in the box;  $N_{\text{rod-strut}}$  is the average number of rigid rods in a strut of the network.

$N$	$L_{\text{box}}$	$L_{\text{ucell}}$	$N_{\text{node}}$	$N / N_{\text{node}}$	$N_{\text{rod-strut}}$
100	12.61	12.61	8	12.5	6.25
400	20.00	12.25	32	12.5	6.25
600	22.92	12.55	52	11.54	5.77
800	25.23	12.12	72	11.11	5.56

Table S2 Average properties of the G phase network for the different lengths of the lateral chain.  $N$  is the number of molecules in the simulation box;  $L_{\text{box}}$  is the length of the simulation box;  $L_{\text{ucell}}$  is the length of the calculated unit cell;  $T^*$  is the temperature range where the G phase is detected;  $N_{\text{node}}$  and  $N_{\text{strut}}$  are the number of nodes and struts of the network in the box;  $N_{\text{rod-strut}}$  is the average number of rigid rods in a strut of the network.

$N_{\text{fix}}$	$\phi_{\text{fix}}$	$N$	$L_{\text{box}}$	$L_{\text{ucell}}$	$T^*$	$N_{\text{node}}$	$N_{\text{strut}}$	$N_{\text{rod-strut}}$
19	0.752	300	20.66	20.66	0.30 ~ 0.95	16	24	12.5
21	0.771	300	21.18	21.18	0.30 ~ 0.90	16	24	12.5
23	0.786	300	21.69	21.69	0.30 ~ 0.95	16	24	12.5
25	0.800	300	22.18	22.18	0.30 ~ 1.00	16	24	12.5
27	0.812	300	22.64	22.64	0.30 ~ 1.05	16	24	12.5
29	0.823	300	23.08	23.08	0.30 ~ 1.00	16	24	12.5

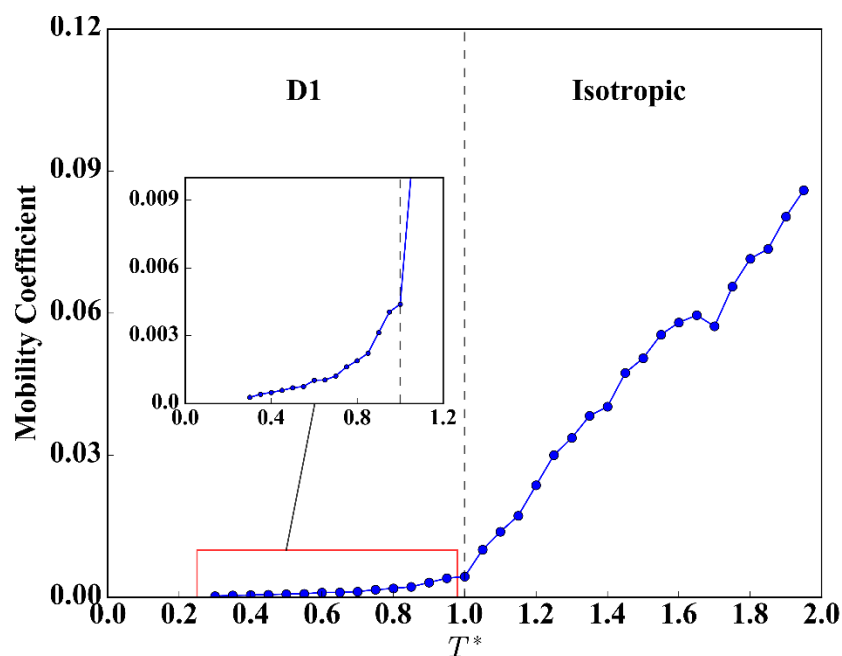


Figure S3 The mobility coefficient for the case of  $N_{\text{fix}} = 11$  and  $N = 600$  as a function of temperature. “D1” refers to the morphology of the “single” diamond phase.

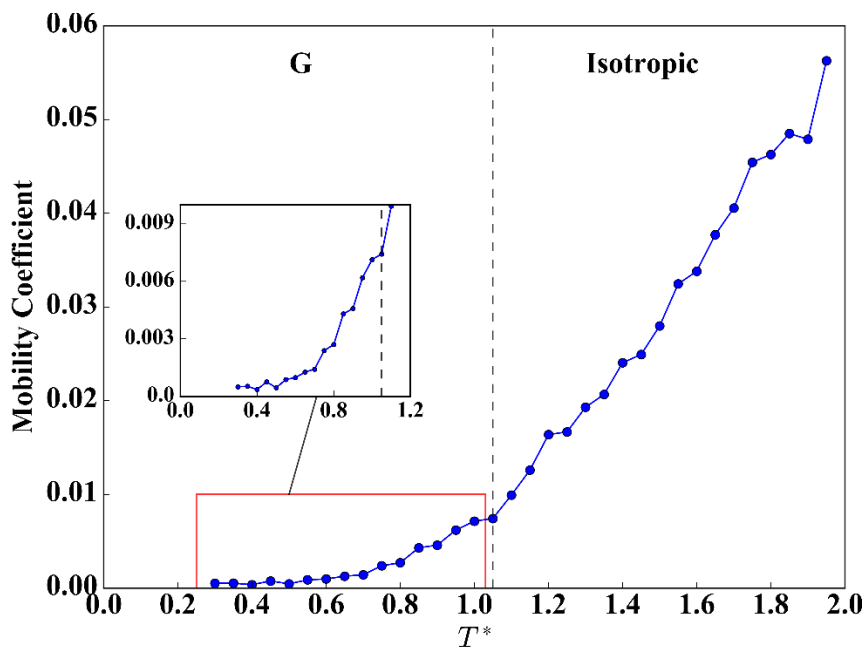


Figure S4 The mobility coefficient for the case of  $N_{\text{flx}} = 19$  and  $N = 300$  as a function of temperature. “G” refers to the morphology of the double gyroid phase.

### Simulation results for TBAs at the packing fraction of $\eta = 0.5$

A series of simulations were performed at a packing fraction of  $\eta = 0.5$ . A global phase diagram in terms of reduced temperature and the volume fraction of the lateral chain ( $\phi_{\text{flx}}$ ) is presented in Figure S5. Compared with the simulation results at  $\eta = 0.45$  shown in Fig. 3, we obtained essentially the same morphologies including the square column, the “single” diamond (D1), the double gyroid (G) and the hexagonal axial-bundle column. The main difference is that for  $\eta = 0.5$  the temperature range of mesophase stability is wider. By increasing the volume fraction, we increased the pressure of the system and the tendency of the molecules to order (*e.g.*, for the rigid rods to align), which shifted the transition point between isotropic phase and LC phase to higher temperatures. The square columnar and the D1 phase are observed at the same  $\phi_{\text{flx}}$  for  $\eta = 0.5$  and  $\eta = 0.45$ . Our simulations did not detect the “single” plumber’s nightmare (P1)

phase at  $\eta = 0.5$ , which was observed at  $\eta = 0.45$ . The G phase was detected for  $0.752 \leq \phi_{flx} \leq 0.786$  at  $\eta = 0.5$ , which is a narrower range than that observed for  $\eta = 0.45$ . The axial-bundle columnar phase was detected for lower  $\phi_{flx}$  values at  $\eta = 0.5$ .

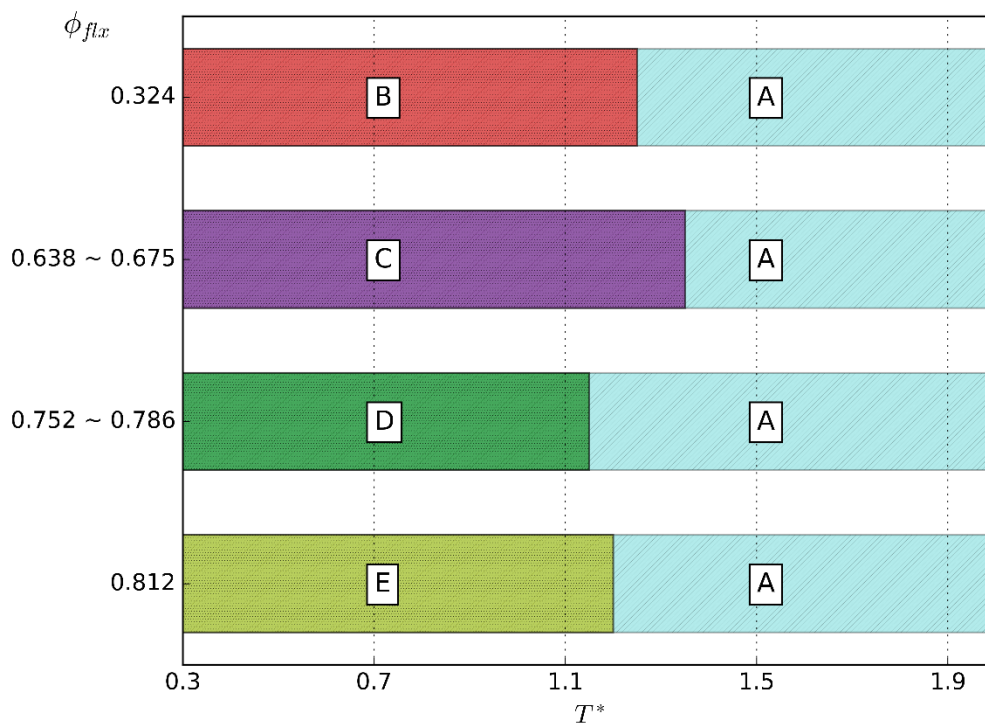


Figure S5 Morphologies obtained in the simulation for the bolaamphiphile molecule with a swallow-tail lateral chain at packing fraction of  $\eta = 0.5$  with the respect to temperature and the volume fraction of the lateral chain. Morphology description: (A) isotropic; (B) square column; (C) ‘single’ diamond network; (D) double gyroid; (E) axial-bundle column.

### Simulations of TBAs of different molecular architecture

To understand the relationship between the architecture of TBA side-chain and the mesophase they form, a series of simulations were performed at  $\eta = 0.45$  for two types of molecules, including the TBA with a linear lateral chain and the TBA with a swallow-tail lateral chain. As shown in Figure S6, for the case of  $N_{flx} = 5, 11$  and  $19$ , TBAs with

either linear or swallow-tail lateral chains will tend to assemble into different morphologies.

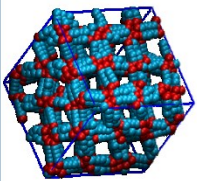
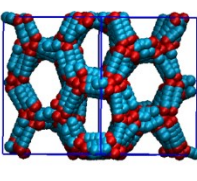
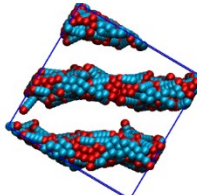
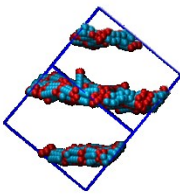
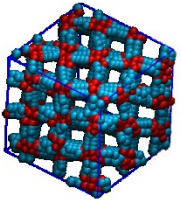
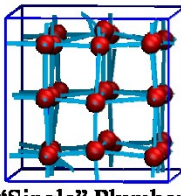
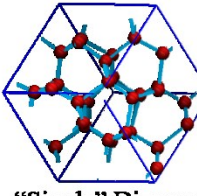
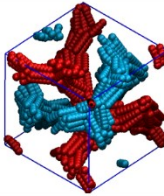
Molecular Architecture	$N_{\text{fix}} = 3$	$N_{\text{fix}} = 5$	$N_{\text{fix}} = 11$	$N_{\text{fix}} = 19$
TBA with a linear lateral chain	 Square Column	 Hexagonal Column	 Lamella (L)	 Lamella (L)
TBA with a swallow-tail lateral chain	 Square Column	 "Single" Plumber's Nightmare (P1)	 "Single" Diamond (D1)	 Double Gyroid (G)

Figure S6 Morphologies obtained for different molecular architecture and various the lengths of the lateral chain. For clarity, only the rigid rods are shown, and only the skeleton of the network is shown in the P1 and D1 phase. Except for the G phase, the type 1 beads are colored red, the type 2 beads are colored blue. For the G phase, two distinct networks, which never intersect, are colored red and blue, respectively.

To investigate the energetic and entropic effects for the same lateral chain architecture in different morphologies, the following method was implemented. We take  $N_{\text{fix}} = 19$  as an example. Figure S6 shows that the L and the G phase were observed for the linear lateral chain TBA (L-TBA) and the swallow-tail lateral chain TBA (S-TBA), respectively. To allow the S-TBA to form the L phase, we take the configuration of the L phase collected from L-TBA, and temporarily "freeze" the position of the rigid rods (*i.e.* by zeroing out the force and torque on the rigid rods). Then we change the harmonic bond between the rigid rod and the lateral chain so as to change the chain topology in a

stepwise manner. At first, this bond connects the rigid rod and the first bead in the lateral chain (the architecture of the L-TBA, see the first picture in Figure S7(a)). We turn off this bond, and add a bond between the rod and the second bead in the lateral chain (see Figure S7(b)). We then allow the system to equilibrate with this new lateral chain architecture over a period of  $t^* = 150000$ . We repeat this process to gradually move the connection from one end to the center of the lateral chain (see Figure S7(c)(d)). Once the rigid rod is connected to the center bead of the lateral chain, we obtain the architecture of the S-TBA in the L phase. Similarly, to allow the L-TBA to form the G phase, we simply “freeze” the rigid rods in the G phase, and change the connection bead of the lateral chain from the center bead to one of the end beads (see Figure S7(e)(f)(g)(h)). To compare the results at the same temperature, we also “freeze” the rigid rods in different morphologies, and gradually change the temperature of the lateral chains toward the target temperature. In this method, we “freeze” the rigid rods throughout the whole procedures, otherwise we won’t get the desired morphology for a specific molecular architecture at a target temperature.

To characterize the conformational behavior of the lateral chain, the end-to-end distance is calculated as illustrated in Figure S8. For the linear lateral chain, the end-to-end distance is defined as the distance between the first and last of the flexible beads. For the swallow-tail lateral chain, the end-to-end distance for each branch is considered, which is defined as the distance between the bead connecting the two branches and the last bead in each branch. Statistics are collected at time intervals of  $\Delta\tau = 500$  over a period of  $t^* = 50000$ , while the rods are frozen to preserve the desired morphology.

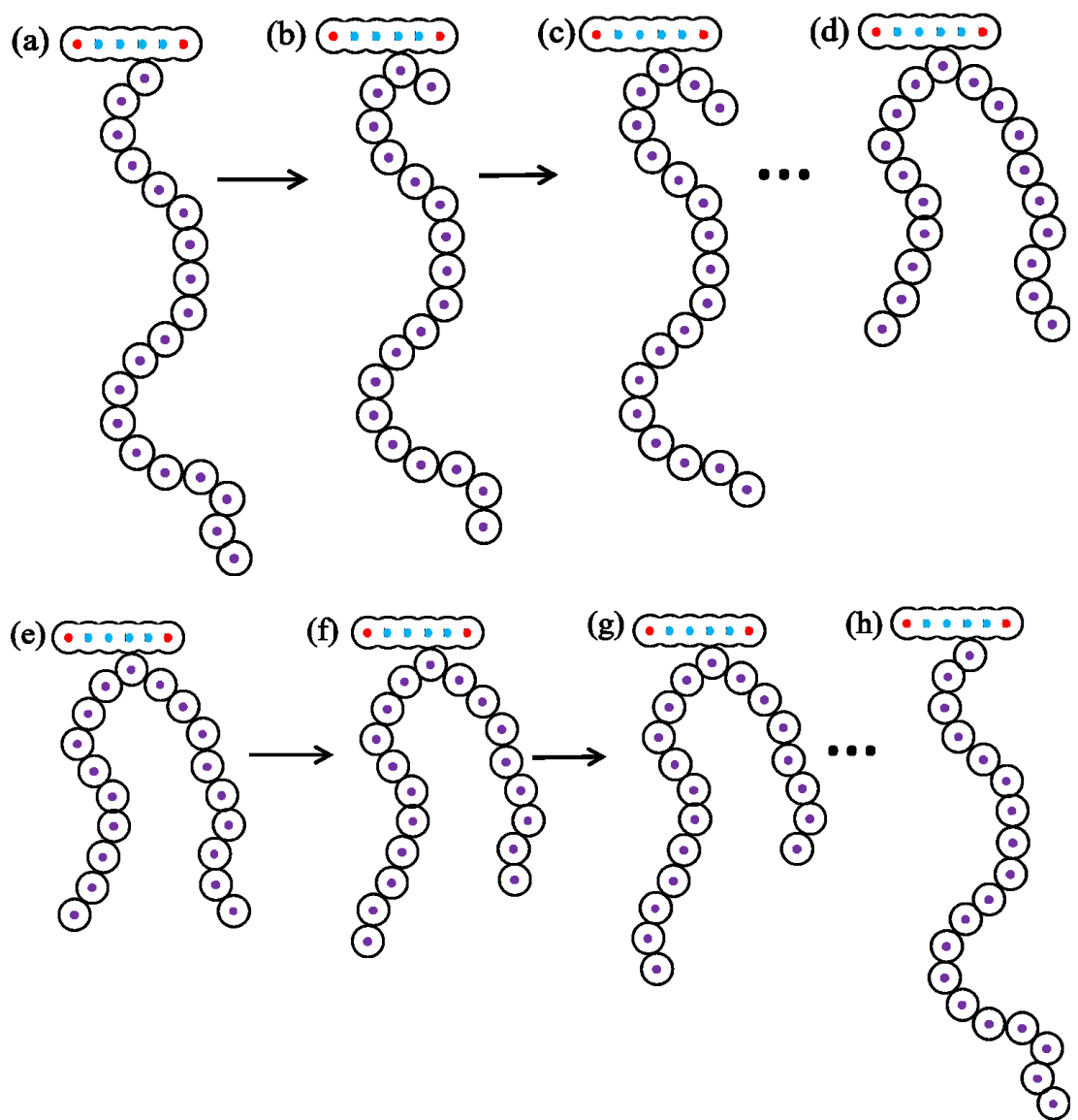


Figure S7 The scheme of changing the lateral chain architecture while “freezing” the rigid rod. (a) to (d) Architecture from L-TBA to S-TBA; (e) to (h) architecture from S-TBA to L-TBA.

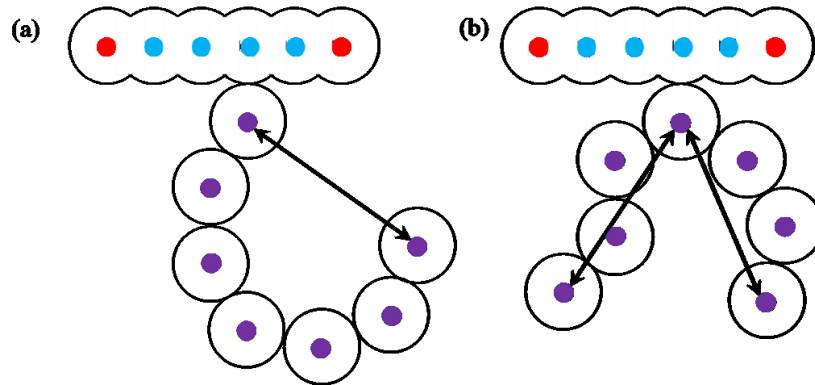


Figure S8 The definition of the end-to-end distance of the lateral chain for the different architecture. Architecture description: (a) TBA with linear lateral chain; (b) TBA with swallow-tail lateral chain.

**(movie; see file P1.avi) Liquid crystalline character of the P1 phase**

A movie is provided that monitors the progression of a system with  $N_{\text{fix}} = 5$  at equilibrium at  $T^* = 0.60$  (LC phase). In the movie, one group of rigid rods are highlighted. At the beginning, these highlighted rigid rods belong to the same strut. During the movie, one of these highlighted rigid rods flips to another strut, while the rest rods still vibrate around the original strut.

**(movie; see file D1.avi) Liquid crystalline character of the D1 phase**

A movie is provided that monitors the progression of a system with  $N_{\text{fix}} = 11$  at equilibrium at  $T^* = 0.80$  (LC phase). In the movie, one group of rigid rods are highlighted. At the beginning, these highlighted rigid rods belong to the same strut. During the movie, one of these highlighted rigid rods flips to another strut, while the rest rods still vibrate around the original strut.

## REFERENCE

- [1] C. Tschierske, C. Nürnberger, H. Ebert, B. Glettner, M. Prehm, F. Liu, X. Zeng and G. Ungar. Complex tiling patterns in liquid crystals. *Interface Focus*, **2**, 669-680 (2012).
- [2] W. Pisula, M. Zorn, J. Young, K. Müllen and R. Zentel. Liquid crystalline ordering and charge transport in semiconducting materials. *Macromol. Rapid Commun.*, **30**, 1179-1202 (2009).
- [3] M. O'Neill and S. M. Kelly. Ordered materials for organic electronics and photonics. *Adv. Mater.*, **23**, 566-584 (2011).
- [4] S. Sergeyev, W. Pisula and Y. H. Geerts. Discotic liquid crystals: a new generation of organic semiconductors. *Chem. Soc. Rev.*, **36**, 1902-1929 (2007).
- [5] L. Maggini and D. Bonifazi. Hierarchized luminescent organic architectures: design, synthesis, self-assembly, self-organisation and functions. *Chem. Soc. Rev.*, **41**, 211-241 (2012).
- [6] E.-K. Fleischmann and R. Zentel. Liquid-crystalline ordering as a concept in materials science: from semiconductors to stimuli-responsive devices. *Angew. Chem. Int. Ed.*, **52**, 8810-8827 (2013).
- [7] J. Dintinger, B.-J. Tang, X. Zeng, F. Liu, T. Kienzler, G. H. Mehl, G. Ungar, C. Rockstuhl and T. Scharf. A self-organized anisotropic liquid-crystal plasmonic metamaterial. *Adv. Mater.*, **25**, 1999-2004 (2013).
- [8] C. H. Yu, C. P. J. Schubert, C. Welch, B. J. Tang, M.-G. Tamba and G. H. Mehl. Design, synthesis, and characterization of mesogenic amine-capped nematic

- gold nanoparticles with surface-enhanced plasmonic resonances. *J. Am. Chem. Soc.*, **134**, 5076-5079 (2012).
- [9] P. Padmanabhan, F. J. Martínez-Veracoechea, J. C. Araque and F. A. Escobedo. A theoretical and simulation study of the self-assembly of a binary blend of diblock copolymers. *J. Chem. Phys.*, **136**, 234905 (2012).
- [10] A. C. Finnefrock, R. Ulrich, G. E. S. Toombes, S. M. Gruner and U. Wiesner. The plumber's nightmare: a new morphology in block copolymer-ceramic nanocomposites and mesoporous aluminosilicates. *J. Am. Chem. Soc.*, **125**, 13084-13093 (2003).
- [11] H. Uehara, T. Yoshida, M. Kakiage, T. Yamanobe, T. Komoto, K. Nomura, K. Nakajima and M. Matsuda. Nanoporous polyethylene film prepared from bicontinuous crystalline/amorphous structure of block copolymer precursor. *Macromolecules*, **39**, 3971-3974 (2006).
- [12] B.-K. Cho, A. Jain, S. M. Gruner and U. Wiesner. Mesophase structure-mechanical and ionic transport correlations in extended amphiphilic dendrons. *Science*, **305**, 1598-1601 (2004).
- [13] S. W. Robbins, P. A. Beaucage, H. Sai, K. W. Tan, J. G. Werner, J. P. Sethna, F. J. DiSalvo, S. M. Gruner, R. B. Van Dover and U. Wiesner. Block copolymer self-assembly-directed synthesis of mesoporous gyroidal superconductors. *Sci. Adv.*, **2**, e1501119 (2016).
- [14] R. L. Kerr, S. A. Miller, R. K. Shoemaker, B. J. Elliott and D. L. Gin. New type of Li ion conductor with 3D interconnected nanopores via polymerization of a

- liquid organic electrolyte-filled lyotropic liquid-crystal assembly. *J. Am. Chem. Soc.*, **131**, 15972-15973 (2009).
- [15] B. A. Pindzola, J. Jin and D. L. Gin. Cross-linked normal hexagonal and bicontinuous cubic assemblies via polymerizable gemini amphiphiles. *J. Am. Chem. Soc.*, **125**, 2940-2949 (2003).
- [16] M. Zhou, P. R. Nemade, X. Lu, X. Zeng, E. S. Hatakeyama, R. D. Noble and D. L. Gin. New type of membrane material for water desalination based on a cross-linked bicontinuous cubic lyotropic liquid crystal assembly. *J. Am. Chem. Soc.*, **129**, 9574-9575 (2007).
- [17] E. J. W. Crossland, M. Kamperman, M. Nedelcu, C. Ducati, U. Wiesner, D.-M. Smilgies, G. E. S. Toombes, M. A. Hillmyer, S. Ludwigs, U. Steiner and H. J. Snaith. A bicontinuous double gyroid hybrid solar cell. *Nano Lett.*, **9**, 2807-2812 (2009).
- [18] E. J. W. Crossland, M. Nedelcu, C. Ducati, S. Ludwigs, M. A. Hillmyer, U. Steiner and H. J. Snaith. Block copolymer morphologies in dye-sensitized solar cells: probing the photovoltaic structure-function relation. *Nano Lett.*, **9**, 2813-2819 (2009).
- [19] M. C. Orilall and U. Wiesner. Block copolymer based composition and morphology control in nanostructured hybrid materials for energy conversion and storage: solar cells, batteries, and fuel cells. *Chem. Soc. Rev.*, **40**, 520-535 (2011).

- [20] R. Dehmel, A. Nicolas, M. R. J. Scherer and U. Steiner. 3D nanostructured conjugated polymers for optical applications. *Adv. Funct. Mater.*, **25**, 6900-6905 (2015).
- [21] J. A. Dolan, M. Saba, R. Dehmel, I. Gunkel, Y. Gu, U. Wiesner, O. Hess, T. D. Wilkinson, J. J. Baumberg, U. Steiner and B. D. Wilts. Gyroid optical metamaterials: calculating the effective permittivity of multidomain samples. *ACS Photonics*, **3**, 1888-1896 (2016).
- [22] M. Stefik, S. Guldin, S. Vignolini, U. Wiesner and U. Steiner. Block copolymer self-assembly for nanophotonics. *Chem. Soc. Rev.*, **44**, 5076-5091 (2015).
- [23] J. A. Dolan, B. D. Wilts, S. Vignolini, J. J. Baumberg, U. Steiner and T. D. Wilkinson. Optical properties of gyroid structured materials: from photonic crystals to metamaterials. *Adv. Optical Mater.*, **3**, 12-32 (2015).
- [24] Z. Almsherqi, F. Margadant and Y. Deng. A look through 'lens' cubic mitochondria. *Interface Focus*, **2**, 539-545 (2012).
- [25] Z. Almsherqi, S. Hyde, M. Ramachandran and Y. Deng. Cubic membranes: a structure-based design for DNA uptake. *J. R. Soc. Interface*, **5**, 1023-1029 (2008).
- [26] S. T. Hyde. Bicontinuous structures in lyotropic liquid crystals and crystalline hyperbolic surfaces. *Curr. Opin. Solid State Mater.*, **1**, 653-662 (1996).
- [27] K. Larsson. Two cubic phases in monoolein-water system. *Nature*, **304**, 664 (1983).

- [28] P. Barois, D. Eidam and S. T. Hyde. X-ray study of cubic phases in ternary systems of surfactant DDAB, water and oil. *J. Phys. (Paris)*, **51(C7)**, 25-34 (1990).
- [29] P. Ström and D. M. Anderson. The cubic phase region in the system didodecyldimethylammonium bromide-water-styrene. *Langmuir*, **8**, 691-709 (1992).
- [30] P. J. Maddaford and C. Toprakcioglu. Structure of cubic phases in the ternary system didodecyldimethylammonium bromide/water/hydrocarbon *Langmuir*, **9**, 2868-2878 (1993).
- [31] J. M. Seddon and R. H. Templer. Cubic phases of self-assembled amphiphilic aggregates. *Phil. Trans. R. Soc. Lond. A*, **344**, 377-401 (1993).
- [32] U. S. Schwarz and G. Gompper. Stability of bicontinuous cubic phases in ternary amphiphilic systems with spontaneous curvature. *J. Chem. Phys.*, **112**, 3792-3802 (2000).
- [33] F. J. Martínez-Veracoechea and F. A. Escobedo. Monte Carlo study of the stabilization of complex bicontinuous phases in diblock copolymer system. *Macromolecules*, **40**, 7354-7365 (2007).
- [34] F. J. Martínez-Veracoechea and F. A. Escobedo. Bicontinuous phase in diblock copolymer/homopolymer blends: simulation and self-consistent field theory. *Macromolecules*, **42**, 1775-1784 (2009).
- [35] B. Yu, B. Li, P. Sun, T. Chen, Q. Jin, D. Ding and A. Shi. Cylinder-gyroid-lamella transitions in diblock copolymer solutions: a simulated annealing study. *J. Chem. Phys.*, **123**, 234902 (2005).

- [36] E. L. Thomas, D. M. Anderson, C. S. Henkee and D. Hoffman. Periodic area-minimizing surfaces in block copolymers. *Nature*, **334**, 598-601 (1988).
- [37] C. Tschierske. Development of structural complexity by liquid-crystal self-assembly. *Angew. Chem. Int. Ed.*, **52**, 8828-8878 (2013).
- [38] S. Kutsumizu. Recent progress in the synthesis and structural clarification of thermotropic cubic phases. *Isr. J. Chem.*, **52**, 844-853 (2012).
- [39] X. Zeng, G. Ungar and M. Imp  rator-Clerc. A triple-network tricontinuous cubic liquid crystal. *Nature Materials*, **4**, 562-567 (2005).
- [40] C. Dressel, F. Liu, M. Prehm, X. Zeng, G. Ungar and C. Tschierske. Dynamic mirror-symmetry breaking in bicontinuous cubic phases. *Angew. Chem. Int. Ed.*, **53**, 13115-13120 (2014).
- [41] M. Vogrin, N. Vaupot  , M. M. Wojcik, J. Mieczkowski, K. Madrak, D. Poci  cha and E. Gorecka. Thermotropic cubic and tetragonal phases made of rod-like molecules. *Phys. Chem. Chem. Phys.*, **16**, 16067-16074 (2014).
- [42] S. N. Chvalun, M. A. Shcherbina, A. N. Yakunin, J. Blackwell and V. Percec. Structure of gyroid mesophase formed by monodenrons with fluorinated alkyl tails. *Polym. Sci. Ser. A*, **49**, 158-167 (2007).
- [43] T. Ichikawa, M. Yoshio, A. Hamasaki, S. Taguchi, F. Liu, X. Zeng, G. Ungar, H. Ohno and T. Kato. Introduction of thermotropic bicontinuous cubic phases in liquid-crystalline ammonium and phosphonium salts. *J. Am. Chem. Soc.*, **134**, 2634-2643 (2012).

- [44] F. Liu, M. Prehm, X. Zeng, C. Tschierske and G. Ungar. Skeletal cubic, lamellar, and ribbon phases of bundled thermotropic bolaamphiphiles. *J. Am. Chem. Soc.*, **136**, 6846-6849 (2014).
- [45] X. Zeng, M. Prehm, G. Ungar, C. Tschierske and F. Liu. Formation of a double diamond cubic phase by thermotropic liquid crystalline self-assembly of bundled bolaamphiphiles. *Angew. Chem. Int. Ed.*, **55**, 8324-8327 (2016).
- [46] C. Tschierske. Liquid crystal engineering – new complex mesophase structures and their relations to polymer morphologies, nanoscale patterning and crystal engineering. *Chem. Soc. Rev.*, **36**, 1930-1970 (2007).
- [47] X. Cheng, M. Prehm, M. K. Das, J. Kain, U. Baumeister, S. Diele, D. Leine, A. Blume and C. Tschierske. Calamitic bolaamphiphiles with (semi)perfluorinated lateral chains: polyphilic block block molecules with new liquid crystalline phase structures. *J. Am. Chem. Soc.*, **125**, 10977-10996 (2003).
- [48] A. J. Crane, F. J. Martínez-Veracoechea, F. A. Escobedo and E. A. Müller. Molecular dynamics simulation of the mesophase behavior of a model bolaamphiphilic liquid crystal with a lateral flexible chain. *Soft Matter*, **4**, 1820-1829 (2008).
- [49] F. J. Martínez-Veracoechea and F. A. Escobedo. Simulation of the gyroid phase in off-lattice models of pure diblock copolymer melts. *J. Chem. Phys.*, **125**, 104907 (2006).
- [50] F. J. Martínez-Veracoechea and F. A. Escobedo. Lattice Monte Carlo simulations of the gyroid phase in monodisperse and bidisperse block copolymer systems. *Macromolecules*, **38**, 8522-8531 (2005).

- [51] T. Dotera. Tricontinuous cubic structures in ABC/A/C copolymer and homopolymer blends. *Phys. Rev. Lett.*, **89**, 205502 (2002).
- [52] J. D. Weeks, D. Chandler and H. C. Andersen. Role of repulsive forces in determining the equilibrium structure of simple liquids. *J. Chem. Phys.*, **54**, 5237-5247 (1971).
- [53] D. Reith, M. Pütz and F. Müller-Plathe. Deriving effective mesoscale potentials from atomistic simulations. *J. Comput. Chem.*, **24**, 1624-1636 (2003).
- [54] M. S. Shell. The relative entropy is fundamental to multiscale and inverse thermodynamic problems. *J. Chem. Phys.*, **129**, 144108 (2008).
- [55] L. Lu, S. Izvekov, A. Das, H. C. Andersen and G. A. Voth. Efficient, regularized, and scalable algorithms for multiscale coarse-graining. *J. Chem. Theory Comput.*, **6**, 954-965 (2010).
- [56] A. Ahmed and R. J. Sadus. Phase diagram of the Weeks-Chandler-Andersen potential from very low to high temperatures and pressures. *Phys. Rev. E*, **80**, 061101 (2009).
- [57] S. J. Plimpton. Fast parallel algorithms for short-range molecular dynamics. *J. Comput. Phys.*, **117**, 1-19 (1995).
- [58] W. Humphrey, A. Dalke and K. Schulten. VMD: visual molecular dynamics. *J. Mol. Graphics*, **14**, 33-38 (1996).
- [59] A. J. Schultz, C. K. Hall and J. Genzer. Obtaining concentration profiles from computer simulation structure factors. *Macromolecules*, **40**, 2629-2632 (2007).

- [60] P. Padmanabhan, F. J. Martínez-Veracoechea and F. A. Escobedo. Computation of free energies of cubic bicontinuous phases for blends of diblock copolymer and selective homopolymer. *Macromolecules*, **49**, 5232-5243 (2016).